Volcanic tremor of the 2010 Eyjafjallajökull eruption

Ásdís Benediktsdóttir [1,2] Ólafur Gudmundsson,[3] Ka Lok Li [3,4] and
Bryndís Brandsdóttir [1]

[1]*Nordic Volcanological Center, Institute of Earth Sciences, University of Iceland, Iceland GeoSurvey, Grensásvegur 9, Reykjavík, Iceland. E-mail:* ab@isor.is
[2]*Iceland Geosurvey, Iceland*
[3]*Department of Earth Sciences, Uppsala University, 752 36 Uppsala, Sweden*
[4]*Geophysics Section, School of Cosmic Physics, Dublin Institute for Advanced Studies, Dublin D04 C932, Ireland*

SUMMARY

Volcanic eruptions in Iceland generally start with an increase in tremor levels. These signals do not have clear onset, like many earthquakes. As the character of the tremor signal is variable from one volcano to another, locating the source of the tremor signal may require different techniques for different volcanoes. Continuous volcanic tremor varied considerably during the course of the Eyjafjallajökull summit eruption, 14 April to 22 May 2010, and was clearly associated with changes in eruptive style. The tremor frequencies ranged between 0.5 and 10 Hz, with increased vigour during an effusive and explosive phase, in comparison with purely explosive phases. Higher-frequency tremor bursts early in the eruption were caused by processes at the eruption site. Location of the tremor using a method based on differential phase information extracted from interstation correlograms showed the tremor to be stable near the eruption vent, through time, for signals between 0.5 and 2 Hz. Analyses of power variations of the vertical component of the tremor with distance from the eruption site are consistent with tremor waveform content being dominated by surface waves in the 0.5–2 Hz frequency range. The tremor source depth was argued to be shallow, less than about 1 km. The attenuation quality factor (Q) was found to be on the order of $Q = 10$–20 for paths in the area around Eyjafjallajökull and $Q = 20$–50 for paths outside the volcano. The pattern of radiated wave energy from the tremor source varied with time, defining ten different epochs during the eruption. Thus the tremor-source radiation did not remain isotropic, which needs to be considered when locating tremor based on amplitude, that is azimuthally variable source radiation.

Key words: Seismic attenuation; Volcano seismology; Volcanic hazards and risks.

1 INTRODUCTION

Understanding the mechanics and behaviour of a volcano forms the basis for managing the risk associated with it. Although both geophysical and geochemical monitoring methods have advanced substantially in recent years, detailed understanding of signals emitted by active volcanoes, is still limited. Elevated levels of seismicity beneath volcanoes have long been interpreted as evidence of magma accumulation or migration (e.g. Hidayati *et al.* 2007; Pedersen *et al.* 2007; Woods *et al.* 2018). Accurate locations of seismic signals originating within an active volcano are important to track movements of magma at depth as well as the propagation of shallow magmatic dikes and sills (e.g. Tarasewicz *et al.* 2012b; Ágústsdóttir *et al.* 2016; Eibl *et al.* 2017a, and references therein).

An abrupt decrease of propagating volcano-tectonic seismicity at the initiation of continuous volcanic tremor has been repeatedly observed at the beginning of volcanic eruptions in Iceland,

for example Surtsey 1963, Heimaey 1973, Krafla during 1975–1984, Hekla 1970, 1980, 1991 and 2000, Bárdarbunga-Gjálp 1996, Grímsvötn 1998, 2004 and 2010 and Holuhraun 2014 (Sigtryggsson & Sigurdsson 1966; Thorarinsson *et al.* 1973; Einarsson *et al.* 1997; Soosalu *et al.* 2005; Vogfjörd *et al.* 2005; Pedersen *et al.* 2007; Jakobsdóttir 2008; Tarasewicz *et al.* 2012a; Ágústsdóttir *et al.* 2016; Eibl *et al.* 2017b; Einarsson 2018; Ágústsdóttir *et al.* 2019). While earthquakes have been clearly related to both lateral and vertical dike propagation, the physical origin of volcanic tremor is not well understood. Eibl *et al.* (2017b) speculate that a swarm of temporally overlapping microseismic events are the cause of the pre-eruptive tremor associated with the 2014 Holuhraun eruption.

Volcanic tremor is a signal recorded at seismic stations in the vicinity of volcanoes and hydrothermal areas. The characteristics of volcanic tremor vary, not only from one volcano to another, but also between eruptions of the same volcano (e.g. Hofstetter &

Malone 1986). For a comprehensive overview of volcanic tremor, see Konstantinou & Schlindwein (2003).

Konstantinou & Schlindwein (2003) defined volcanic tremor as 'a persistent seismic signal that is observed only near active volcanoes, lasting from several minutes to several days, preceding and/or accompanying most volcanic eruptions' (Fehler 1983; Julian 1994; Ripepe 1996; Métaxian *et al.* 1997). Volcanic tremor is usually attributed to fluid movement within the volcano. Such signals have been modelled as: fluid-filled tensile-cracks (Aki *et al.* 1977), in which tremor is produced by an excess pressure in the magma that results in a jerky opening of the crack; as a non-linear excitation by fluid flow (Julian 1994); as an acoustic resonance of a fluid-filled volcanic pipe triggered by excess gas pressure (Chouet 1985); as a continuous bursting of small gas bubbles in the upper part of the magmatic column (Ripepe 1996); and as repeating occurrence of long-period or stick-slip events (e.g. Neuberg *et al.* 2000; Hotovec *et al.* 2013). Although the cause of volcanic tremor is not always the same, it is usually attributed to magma movement related to ongoing processes at a volcano at any given time. Therefore, analyses of tremor can give valuable insights into magma dynamics within a volcano.

The character of tremor signals varies; it can be characterized by a fundamental frequency and its harmonics (e.g. Mt Semeru, Schlindwein *et al.* 1995), a monochromatic peak (e.g. Mt Ruapehu Hurst 1992), tremor bursts with quiescence in between (e.g. Mt Miyakejima Fujita 2008), continuous tremor with varying amplitude (e.g. Mt Krafla Brandsdóttir & Einarsson 1992) or by a series of long-period earthquakes that occur so densely in time that they merge into a continuous tremor signal (Neuberg *et al.* 2000; Baptie *et al.* 2002). Also, tremor signal from the same eruption can have different sources like Eibl *et al.* (2017b) found in the 2014 Holuhraun eruption, Iceland. These are only a few examples of how volcanic tremor has been classified.

Locating volcanic tremor is not possible using standard arrival time methods as it does usually not have a clear onset. There are a few exceptions (Aki *et al.* 1977; Fehler 1983). Also, the heterogeneity of volcanoes and potentially strong site effects (e.g. topography) add to the complexity of the location problem. Therefore, other techniques have been developed to locate the tremor sources. These include analysis of amplitude decay of the signal with distance from the source (e.g. Gottschämmer & Surono 2000; Battaglia & Aki 2003; Di Grazia *et al.* 2006), where the source is assumed to radiate isotropically. If the source behaves as such, the method works well. However, this is not always the case, as in the 2010 Eyjafjallajökull summit eruption, reported in this paper.

Exploiting differential-phase information by waveform-semblance and beam-forming methods across a dense array of seismographs (e.g. Furumoto *et al.* 1990, 1992; Wassermann 1997; Eibl *et al.* 2017a) or by cross correlating adjacent recordings of tremor (Gudmundsson & Brandsdóttir 2010; Ballmer *et al.* 2013; Droznin *et al.* 2015; Li *et al.* 2017b, a; Sgattoni *et al.* 2017) has proven to work well in several areas in order to locate tremor sources. In the former, the direction to the source and wave velocity or slowness are determined. In the latter, the time series from two seismographs in the vicinity of the tremor source(s) are cross-correlated to reveal the signal at the time delay that corresponds to the differential distance from the dominant source to the two receivers. If the tremor contains significant surface wave energy and a suitable surface wave speed is used, the correlograms can be back projected two dimensionally and stacked to reveal an image map of possible source locations (Li *et al.* 2017a).

Here we analyse tremor associated with the 2010 Eyjafjallajökull summit eruption. First, tremor is located with a probabilistic inference method based on interstation correlograms (Section 5.2). Secondly, the power-spectral amplitude of the tremor is analysed to estimate wave attenuation (Section 6.1), the geometrical spreading of the tremor waves (Section 6.2) and station corrections combining propagation and site effects (Section 6.3). Spectral amplitudes relative to a fixed reference station vary with time indicating that the power-radiation pattern of the source varies with time.

2 EYJAFJALLAJÖKULL VOLCANO

Eyjafjallajökull is a 1651 m high east–west oriented stratovolcano (Fig. 1), partly covered by a glacier. It is located in southern Iceland, next to the subglacial Katla volcano. It extends 25 km in the east–west direction, 15 km in the north–south direction, and its southern cliffs lie only a few kilometres from Iceland's southern coastline. Its caldera is small, only 2.5 km wide, and ice filled.

Four known eruptions have occurred in Eyjafjallajökull during the past 1200 yr, including the most recent in 2010. In the 10th century a trachytic lava eruption with mafic and silicic tephra components formed the NW trending Skerin ridge (Óskarsson 2009) about 2 km WNW from the caldera. A poorly described eruption took place in 1612 or 1613 (Jónsson 1774; Larsen *et al.* 1999). A summit eruption between December 1821 and January 1823 produced highly silicic magma (Larsen *et al.* 1999; Gudmundsson *et al.* 2010).

In the past 30 yr, four periods of unrest have taken place in Eyjafjallajökull. In 1994 and 1999–2000 earthquakes and uplift were recorded and modelled as two horizontal sill intrusions (Dahm & Brandsdóttir 1997; Sturkell *et al.* 2003; Pedersen & Sigmundsson 2004, 2006; Hooper *et al.* 2009) and in 1996 a deep earthquake swarm at 20–25 km depth was detected (Hjaltadóttir *et al.* 2015). Two eruptions took place in 2010, first an effusive eruption at Fimmvörduháls on the eastern flank of the volcano (F in Fig. 1), then a mostly explosive eruption in the summit caldera of Eyjafjallajökull (E in Fig. 1). Prior to the two eruptions uplift and enhanced seismicity were recorded (Sigmundsson *et al.* 2010; Tarasewicz *et al.* 2011, 2012a, 2014).

Gudmundsson *et al.* (2012) divided the 2010 Eyjafjallajökull eruption into four phases based on a combination of various data sets, including tephra fallout data, tephra dispersal outside Iceland and plume height (Table 1).

3 DATA

The data used in this study come from 12 seismographs (see Fig. 1), six of which (*bas*, *esk*, *god*, *mid*, *hvo*, *hau*) are a part of the SIL network operated by the Icelandic Meteorological Office (IMO) and six (*bar*, *fag*, *fim*, *gig*, *sel*, *nup*) were temporarily deployed by the Institute of Earth Sciences, University of Iceland. The station locations are listed in Table 2 together with their distance and azimuth from the summit eruption site. All stations were equipped with Lennartz 5 s seismometers except for station god that had a broad-band GURALP CMG-3ESPC seismometer. The SIL stations record continuous data, with some short gaps due to data transmission problems, to a central recording facility. The temporary stations were all deployed before the beginning of the eruption, except for station bar that was deployed on 9th May. Short gaps occurred at most of the temporary stations due to power outages. Fig. 2 shows
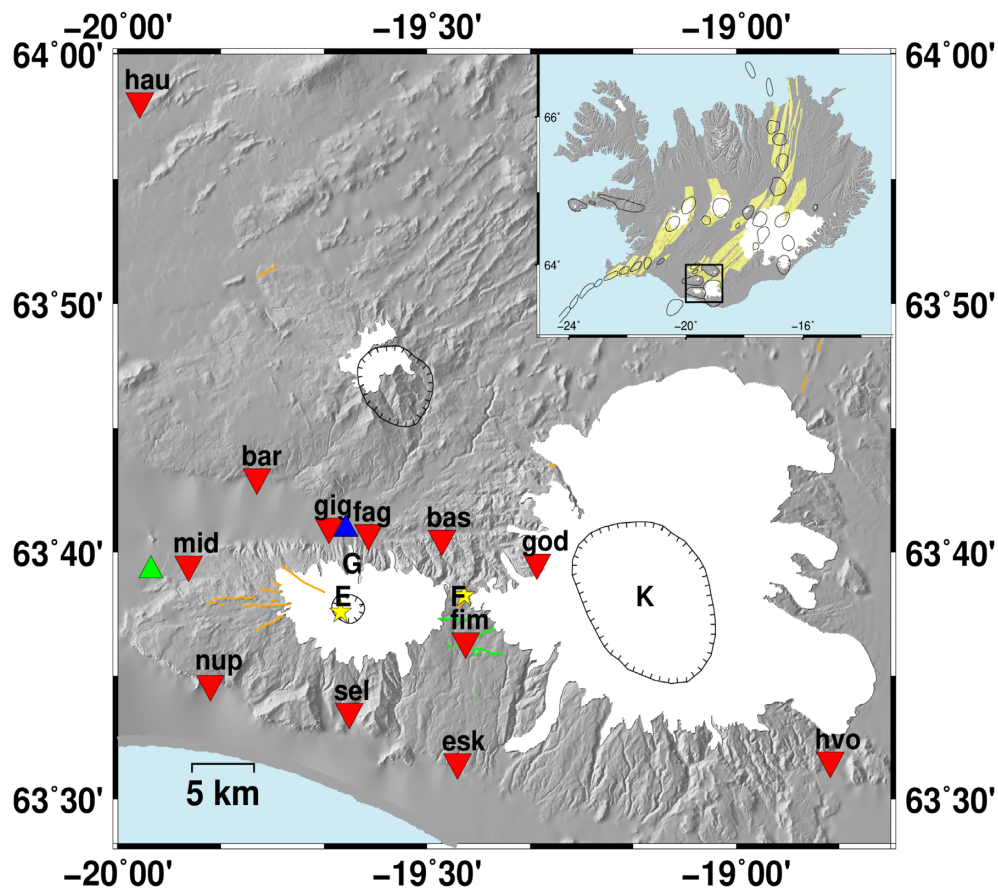
Figure 1. Observation sites and setting of Eyjafjallajökull. Red inverted triangles are seismic stations, green and blue triangles are the Markarfljót and Gígjökulsárlón flood gauges, respectively, and solid and hatched lines are outlines of central volcanic systems and calderas, respectively. E = Eyjafjallajökull, F = Fimmvörduháls, K = Katla, G = Gígjökull. Yellow stars indicate locations of the eruption sites of the flank eruption on Fimmvörduháls and the summit eruption of Eyjafjallajökull. Orange and green lines are eruptive fissures and faults, respectively [data compiled by Einarsson & Hjartardóttir (2015), see references therein].

Table 1. Phases of the eruption as described by Gudmundsson *et al.* (2012).

Phase	Duration	Description
I	April 14–18	First explosive phase including several hours of jökulhlaups (meltwater floods) on April 14–15.
II	April 18–May 4	Effusive-explosive phase. Weak explosive activity and lava effusion as a 3-km-long lava flow formed when magma flowed towards the north out of the caldera
III	May 5–17	Second explosive phase. A new explosive phase with a change in melt composition.
IV	May 18–22	Final phase. The power from the eruption steadily decreased.

Table 2. Station locations, distances and azimuths relative to the summit eruption site at (−19.6365,63.629, Magnússon *et al.* 2012).

Station	Longitude	Latitude	Elevation [m]	Dist. from eruption site [km]	Azimuth from eruption site Degrees east of north
bas	63.67570	−19.47592	300	9.5	56
bar	63.71702	−19.77526	130	11.9	326
esk	63.52503	−19.45080	100	14.7	140
fag	63.67951	−19.59486	200	6.0	21
fim	63.60665	−19.43766	860	10.1	102
god	63.65976	−19.32236	1200	15.9	77
gig	63.68388	−19.65865	162	6.2	350
hau	63.52610	−18.84781	200	40.6	337
hvo	63.96851	−19.96471	100	41.1	106
mid	63.65833	−19.88573	130	12.7	286
nup	63.57787	−19.85037	30	12.0	243
sel	63.55901	−19.62575	70	7.8	175

the recording history of the stations in vertical component spectrograms covering the eruption period. All stations were operated at 100 samples per second with GPS timing. All records were calibrated in physical units (μm s^{-1}) and the response of the single broad-band instrument replaced by that of a Lennartz 5 s sensor. Further processing steps were taken in some parts of the analyses and they are described where applicable in subsequent text. In the body of this paper we present results based on the vertical (Z) component recordings of 11 seismographs. We do not use station gig in other than the initial analyses as it was dismantled 2 d into the eruption. Results based on the horizontal components are presented in Appendices.

4 THE EYJAFALLAJÖKULL TREMOR

Tremor associated with the 2010 Eyjafjallajökull summit eruption was first recorded at the onset of the eruption. The tremor continued throughout the eruption (14 April to 22 May 2010) with variable intensity and faded towards its end. It was characterized by a broad frequency range up to 10 Hz at stations close to the source (Fig. 2). Tremor levels at stations, 40 km away from the eruption site, exceeded the background noise during the first two phases of the eruption (Table 1). Time invariant spectral peaks appear as horizontal bands in the spectrograms in Fig. 2, sometimes extending throughout the eruption period, for example spectral peaks between 0.8 and 2 Hz at most of the near-field stations. Variations in the tremor intensity at different stations are dependent on attenuation along the propagation path. Spectral peaks become less clear when the power of the eruption declines, and do not correlate in frequency for all stations. This may be due to resonances in the propagation process

The temporal evolution of tremor amplitude spanning the four phases of the eruption is shown at two seismic stations (fag and nup) in Figs 3(a) and (b). Here the amplitude is the rms amplitude over 1-hr time windows, without any overlap. The time evolution displays a distinct character within each phase of the eruption. During the first explosive phase (I) the tremor amplitude was highly variable. In particular two distinct and short-lived ($\approx$2 hr) peaks are apparent in Figs 2, 3(a) and (b) that occurred on 14 April and late on 15 April (see details in Fig. 4).

During the 17-day-long effusive-explosive phase II the amplitude of the tremor was high and relatively stable. The lava advanced slowly within the summit region ($<$100 m d^{-1}) during April 18–26, thickening to 80–100 m under ice that was initially 150–200 m thick (Oddsson *et al.* 2016). During April 30 to May 4 a more rapid advance (up to 500 m d^{-1}) formed a thinner (10–20 m) lava flow on the slopes outside the caldera where the ice was 60–100 m thick (Oddsson *et al.* 2016). Interestingly, during the slow advance of the lava the tremor in the 0.5–1 Hz band decreased gradually, but during the faster advance of the lava, the tremor slowly increased again with time.

During the explosive phase III the tremor amplitude decayed steadily and during phase IV it dropped rapidly after an initial, short stable period.

The temporal evolution of the tremor during the first 2.5 d of the eruption is shown in Fig. 4. The first signs of an imminent eruption was an intense microearthquake swarm at 22:30 on 13th April (Tarasewicz *et al.* 2012a; Karlsdóttir *et al.* 2012, 1 in Fig. 5), with earthquake locations clustered at 4–5 km depth within the caldera (Tarasewicz *et al.* 2012a). Shortly after that, at 23:00, another microearthquake swarm started at about 1 km depth followed

by elevated tremor levels (1a in Fig. 5). As microearthquake activity ceased tremor levels became steady at approximately 1:10 on 14th April (2 in Fig. 5). As stated in the introduction, character such as this, ceasing microearthquake activity and increasing tremor levels, are a signs of the start of an eruption. Therefore, we assume that the eruption started at this time.

Magnússon *et al.* (2012) compiled the detailed course of events during the first few days of the eruption using SAR images, including observations of jökulhlaups (meltwater floods) associated with glacier melting. Four main tremor peaks are observed (T1, T2, T3 and T4 in Figs 4a–c). These can also be seen in spectrograms (Fig. 2) at the very beginning as two vertical bands. Discharge data (Icelandic Meteoroglogical Office 2019b) from a gauge in Markarfljót (see location of the gauge in Fig. 1) shows four main flood peaks (Fig. 4d). The first two flood peaks occurred on 14th April, at about 11:20 and 19:10 for the first and second flood peaks, respectively. The third flow peak occurred at about 20:00 on 15th April and the fourth one near midnight on 16th April. A more detailed discussion on the tremor during the first 2.5 d is in the discussion section.

5 TREMOR LOCATION

5.1 Locating tremor with probabilistic inference

Earthquakes have a clear onset, which is used to locate them. Tremor-like signals do not have a clear onset and several methods, using differential-phase information, have recently been presented in the literature to locate such signals. A number of the methods are variations of the same theme that exploits the correlation of pairs of recordings of the tremor signal. This yields information about differential distance to the tremor source (Haney 2010; Gudmundsson & Brandsdóttir 2010; Ballmer *et al.* 2013; Droznin *et al.* 2015; Sgattoni *et al.* 2017). A common feature of these methods is that some attribute of the correlograms (e.g. their envelope functions) is back projected in two-dimensions and stacked to construct an image of the source (distribution). These methods can be regarded as imaging methods (imaging apparent back-projected energy emission) and do not provide direct information about uncertainty.

Li *et al.* (2017b) introduced double correlation to suppress correlated noise in the correlograms. They simulated test tremor from the Katla volcano (Sgattoni *et al.* 2017) in terms of a primary source and multiple scattered phases (with random orientation, random amplitude, random scattering width). The correlogram envelopes appear as a distributed signal with oscillatory decay away from a central maximal peak at the time shift of the primary source. The scattered content of the tremor constitutes noise in the correlograms from the perspective of locating the source(s) that is partially correlated from one correlogram to another. They also showed, by a synthetic study, that if the back projection is done with a suitable surface wave velocity, it suffices that the tremor contains a significant amount of energy in surface waves, that is it need not be dominated by surface waves. This is because any potential body wave component of the tremor signal will not be back projected coherently and therefore does not stack constructively. Li *et al.* (2017a) went further to introduce higher-order products of correlograms (than the second order of double correlation), thereby achieving further suppression of correlated noise in the correlograms.

Li & Gudmundsson (2020) further verified that tremor at Katla volcano could be simulated in terms of a primary source and multiple scattered phases and cast the location task in probabilistic terms. They applied Bayes Rule to map the correlogram envelopes
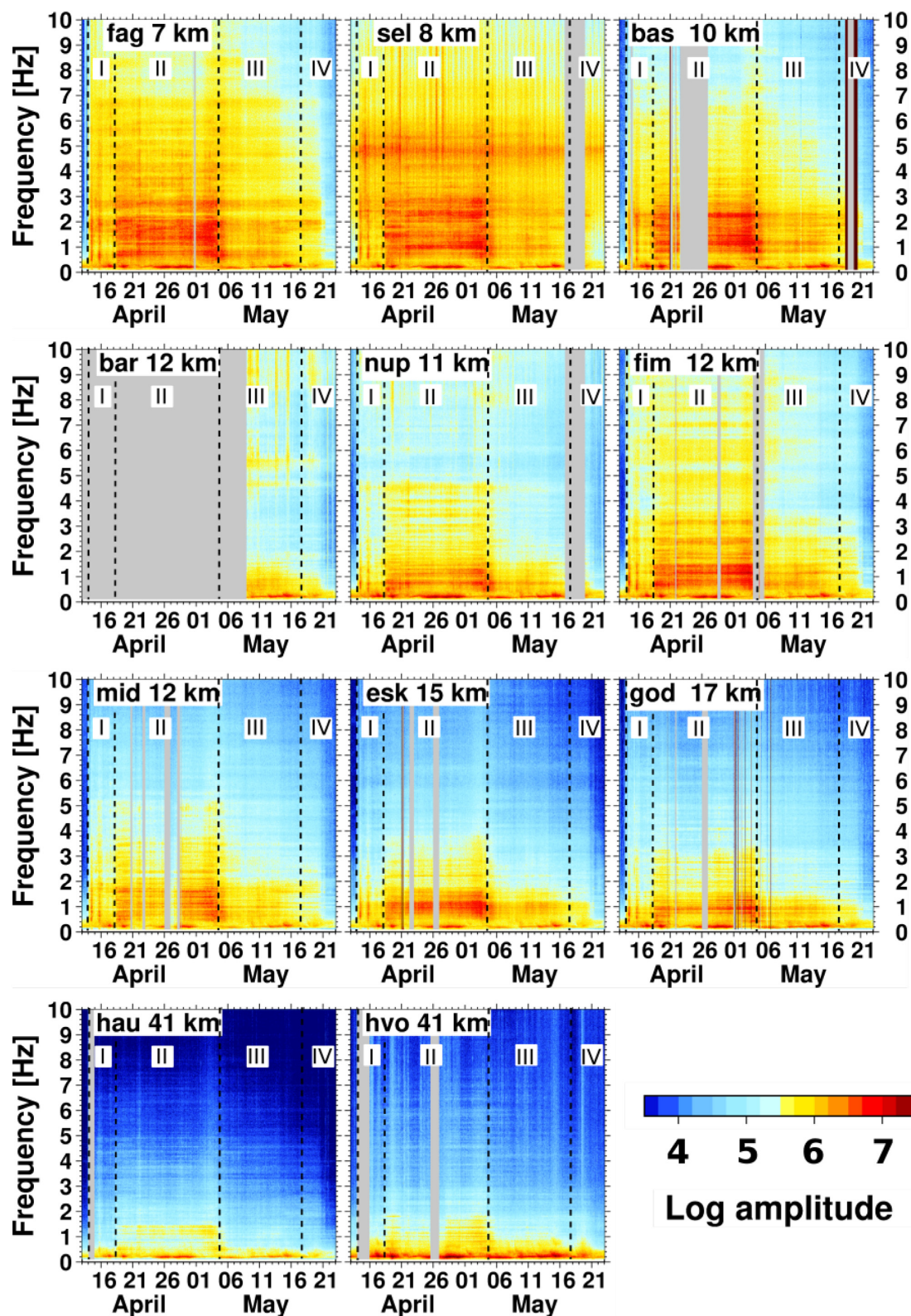
Figure 2. Z-component spectrograms spanning the entire eruption period for all eleven stations used. The station name and distance from the eruption site is given in each frame. The spectrograms were calculated using hour-long windows. The secondary microseisms are visible in the spectrograms with a peak at 0.2 Hz. The phases of the eruption (I–IV) are separated with a black dashed line.
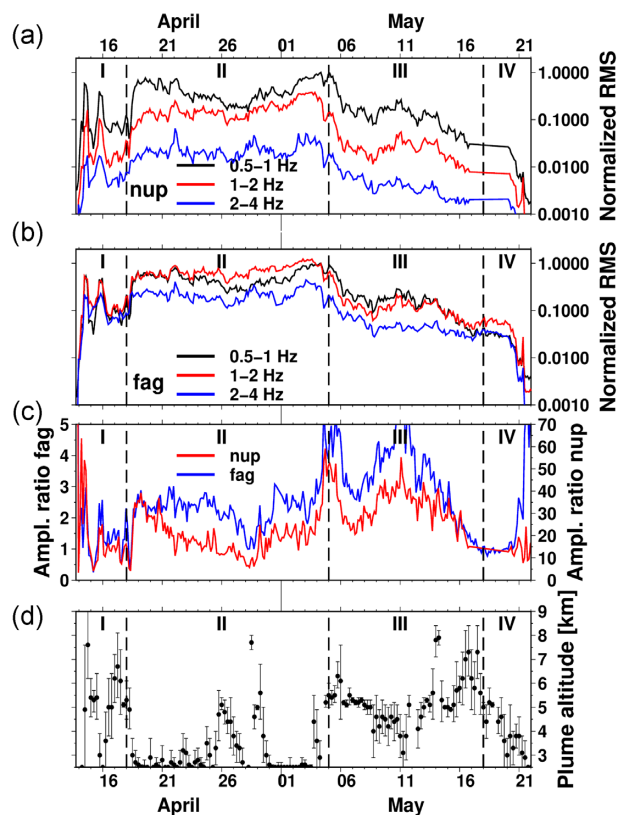
Figure 3. Semi-log plots of normalized 1-hr-RMS amplitudes during the 2010 Eyjafjallajökull summit eruption for stations nup (a) and fag (b) for three different frequency ranges [0.5–1 Hz (black), 1–2 Hz (red) and 2–4 Hz (blue)], normalized by the maximum amplitude of the 0.5–1 Hz frequency range. They are normalized for a better comparison between stations. (c) Ratio between the 1-hr-RMS for the 0.5–1 and 2–4 Hz during the course of the eruption for nup (red) and fag (blue). Note that the scales for the two stations are different. (d) A 6-hr average of the top height of the eruption plume (km a.s.l.). The bars represent one standard deviation. Data from Arason *et al.* (2011). Four different phases, as defined by Gudmundsson *et al.* (2012), are indicated (I–IV).

into a probability density based on the distribution of its noise. Subsequently, they mapped this probability density into a likelihood function for location of the primary source of the tremor given a single correlogram. Finally, the product of all such single-correlogram likelihood functions yields the total likelihood for the tremor location assuming that different correlograms give independent information. Their method can be seen as an inference method since it yields a location estimate as well as an indication of its uncertainty.

We find that correlograms of the Eyjafjallajökull tremor have similar characteristics to those of tremor at nearby Katla and applied the method of Li & Gudmundsson (2020) to locate the primary source of the Eyjafjallajökull tremor. Before calculating cross correlations the mean of each seismogram was removed and the data were low-pass filtered at 4 Hz and then decimated from 100 to 10 samples per second. Data were corrected for instrument response and a 1-bit, time-domain normalization was applied. Seismograms were then correlated. The frequency content of the tremor signal overlaps with the secondary microseisms that peak at roughly 0.2 Hz (Fig. 2). The lower limit of the lowest frequency band to be analysed was chosen at 0.5 Hz in order to avoid overlap with the microseisms. The correlograms were filtered in three frequency bands; 0.5–1 Hz, 1–2 Hz
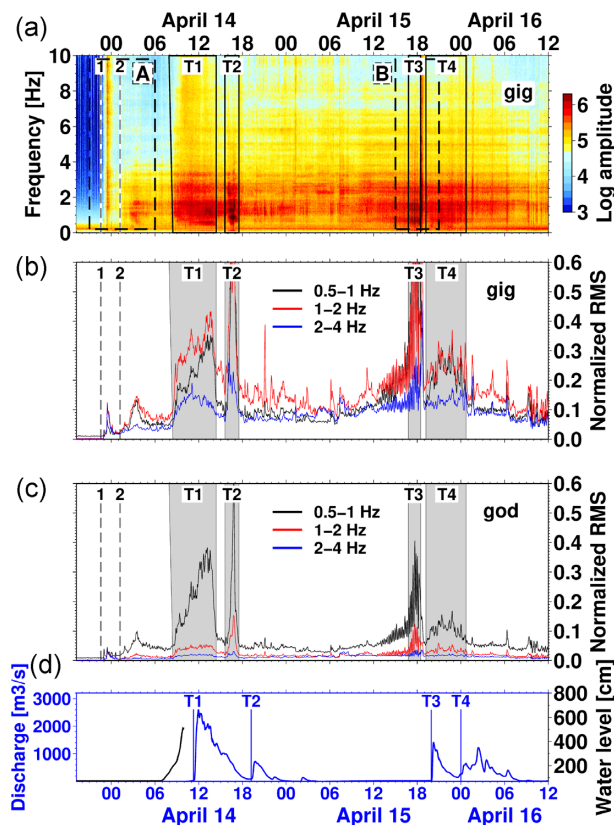

Figure 4. Course of events during the first 2.5 d of the eruption. (a) Spectrogram from the station gig, calculated from 2-min-long windows. Dashed boxes outline time-span of parts A and B of Fig. 5. Black boxes outline the four tremor pulses observerd, T1–T4. **B** Root mean square amplitude over 2 minutes for stations gig. Black, red and blue are the 0.5–1 Hz, 1–2 Hz and 2–4 Hz frequency bands, respectively, normalized by the maximum amplitude of the 0.5-1 Hz at station gig. Shaded areas indicate four tremor pulses observed, T1–T4. 1 and 2 refer to the onset of an microearthquake swarm and the onset of the eruption (Karlsdóttir *et al.* 2012) when tremor levels increased considerably. **C** Same as **B** at station god. **D** Flow data from a gauge in Markarfljót (Icelandic Meteoroglogical Office 2019b) (blue) and water level at a gauge just north of Gígjökull (black) (Icelandic Meteorglogical Office 2019a), see gauge locations in Fig. 1. The gauge just north of Gígjökull washed away with the first flood. Flow peaks T1–T4 correlate fairly well with the corresponding tremor peaks. See text for detail.

and 2–4 Hz. Examples of the temporal evolution of the envelopes of daily correlograms are shown in Fig. 6 for two station pairs. The character is different for the three frequency bands shown, with the signal becoming more complex as frequency increases. The signal is very stable for the 0.5–1 Hz band (Figs 6a and b) during the course of the eruption. This is also the case for the 1–2 Hz band (Fig. 6c) for the majority of the station-pairs, although a few pairs exhibit a little more complexity (e.g. mid-fag, Fig. 6d) where a shift to larger negative differential time is suggested at the very end of the eruption. In the 2–4 Hz band, the signal spans a broader range of time shifts, which we attribute to enhanced scattering with increased frequency. Again, the correlograms for station pair mid-fag suggest a shift to larger negative time shifts at the end of the eruption. It is in this highest frequency range that the temporal changes in the signal correlate best with the eruption history as defined by Gudmundsson *et al.* (2012, Figs 6e and f).

The stations used for locating the tremor were the ones closest to the eruption site (bas, esk, fag, fim, god, nup, mid, sel) as the signal
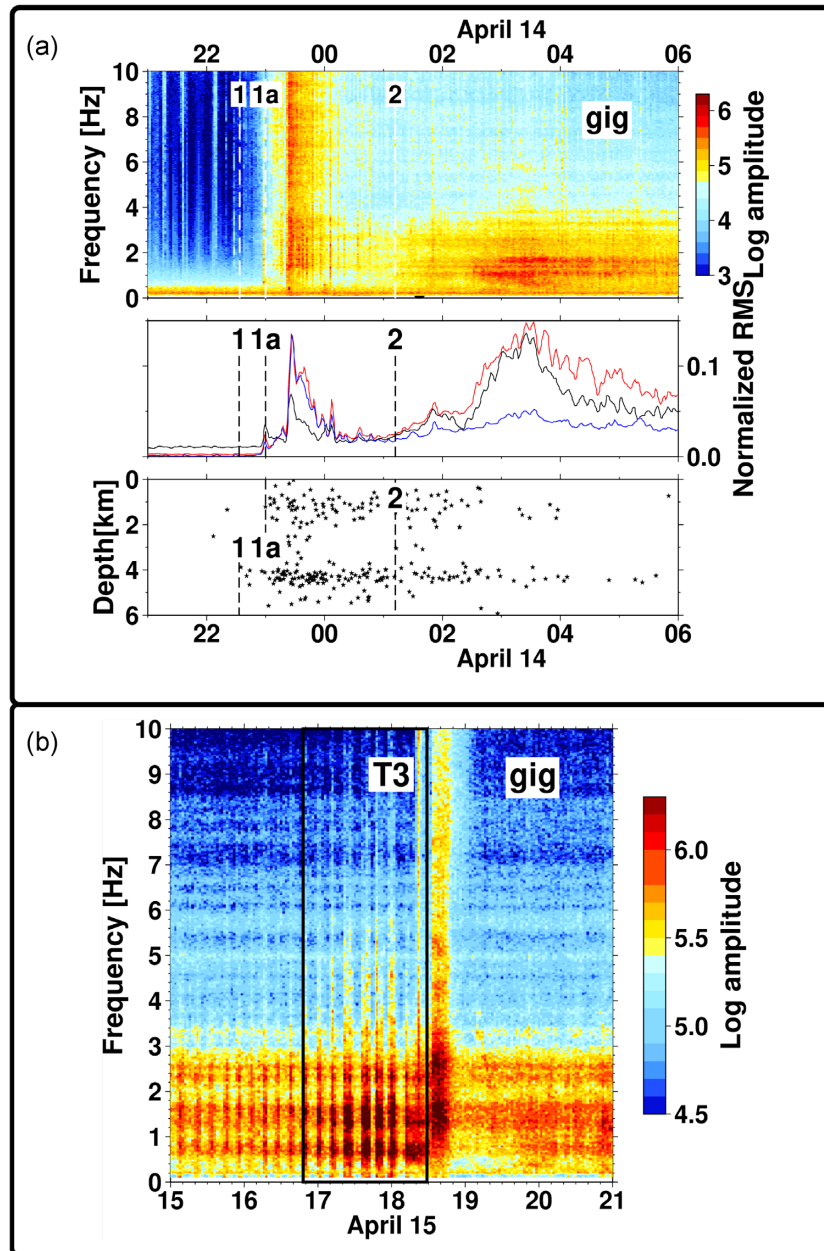
Figure 5. (a) Amplitude spectra on 14th April for the first few hours of the eruption at station gig (top panel), normalized RMS for station gig (colours and normalization as in Fig. 4b); (middle panel) and depth of earthquakes in the caldera (from Tarasewicz *et al.* (2012a)). Note decrease in hypocentral depth at 1a and diminishing seismic activity prior to the onset of the eruption at 2. (b) Spectrogram of station gig during tremor pulse T3 (black box) on 15th April. The spectrograms were computed using 2-min-long windows. See text for details.

in the cross correlations for pairs including stations farther away (>40 km) was weaker and less distinct. A homogeneous velocity distribution was used for the back projection. In the method of Li & Gudmundsson (2020) the envelopes of the correlogram is back projected in two dimensions. Therefore, the appropriate choice of velocity is group velocity of a surface wave. We used group velocities of $v = 1.4$, 1.3 and 1.2 km s^{-1} for the 0.5–1 Hz, 1–2 Hz and 2–4 Hz frequency bands, respectively. These velocities are smooth extrapolations of the phase-velocity measurements reported by Benediktsdóttir *et al.* (2017) from Eyjafjallajökull and from nearby Katla and their group-velocity measurements (Jeddi 2018, personal communication). These choices of velocity also focus the location-likelihood functions optimally for the respective frequency

bands. Varying the velocity by 0.1 km s^{-1} changed the outcome less than by a few hundred metres for the two lower frequency bands, but the change of the outcome for the 2–4 Hz frequency band was greater, on the order of a kilometre.

5.2 Tremor location: results

We experimented with locating the tremor with single-day correlograms at the high-resolution end to correlograms for the whole duration of the eruption at the other extreme. The likelihood of the tremor location from eruption-long correlograms is shown in Figs 7(a)–(c). The same method was applied to daily correlograms for all the days of the eruptions. The difference between the daily
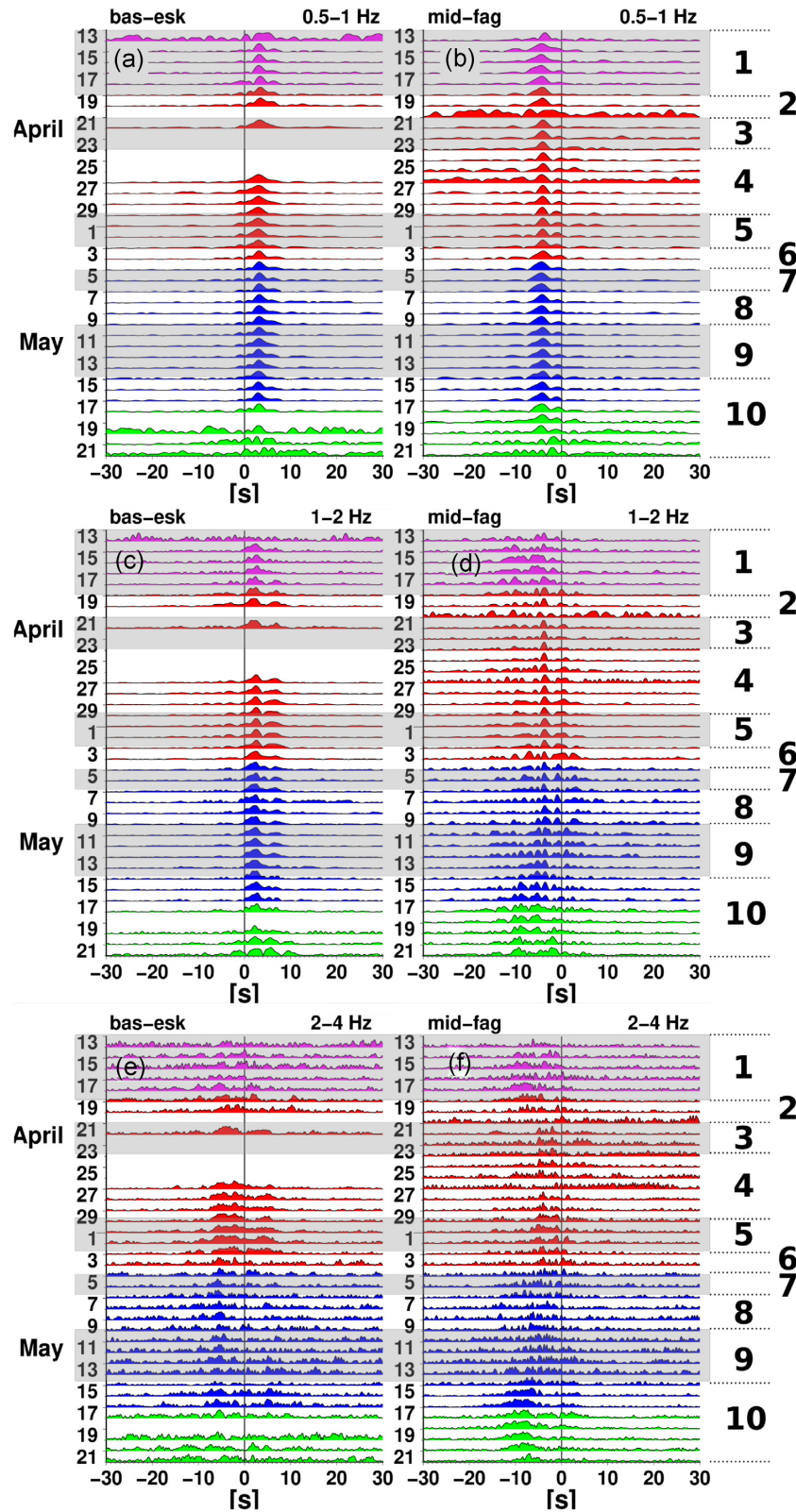
Figure 6. Correlograms for station pairs bas-esk (a, c, e) and mid-fag (b, d, f) at 0.5–1 Hz, 1–1 Hz and 2–4 Hz, during the course of the eruption. Each colour represents a different phase of the eruption as defined by Gudmundsson *et al.* (2012); phases I, II, II and IV are purple, red, blue and green, respectively. Ten time intervals defined in Section 5 based on power ratios at the different stations are grey shaded and indexed on the right hand side (see also Table 3).
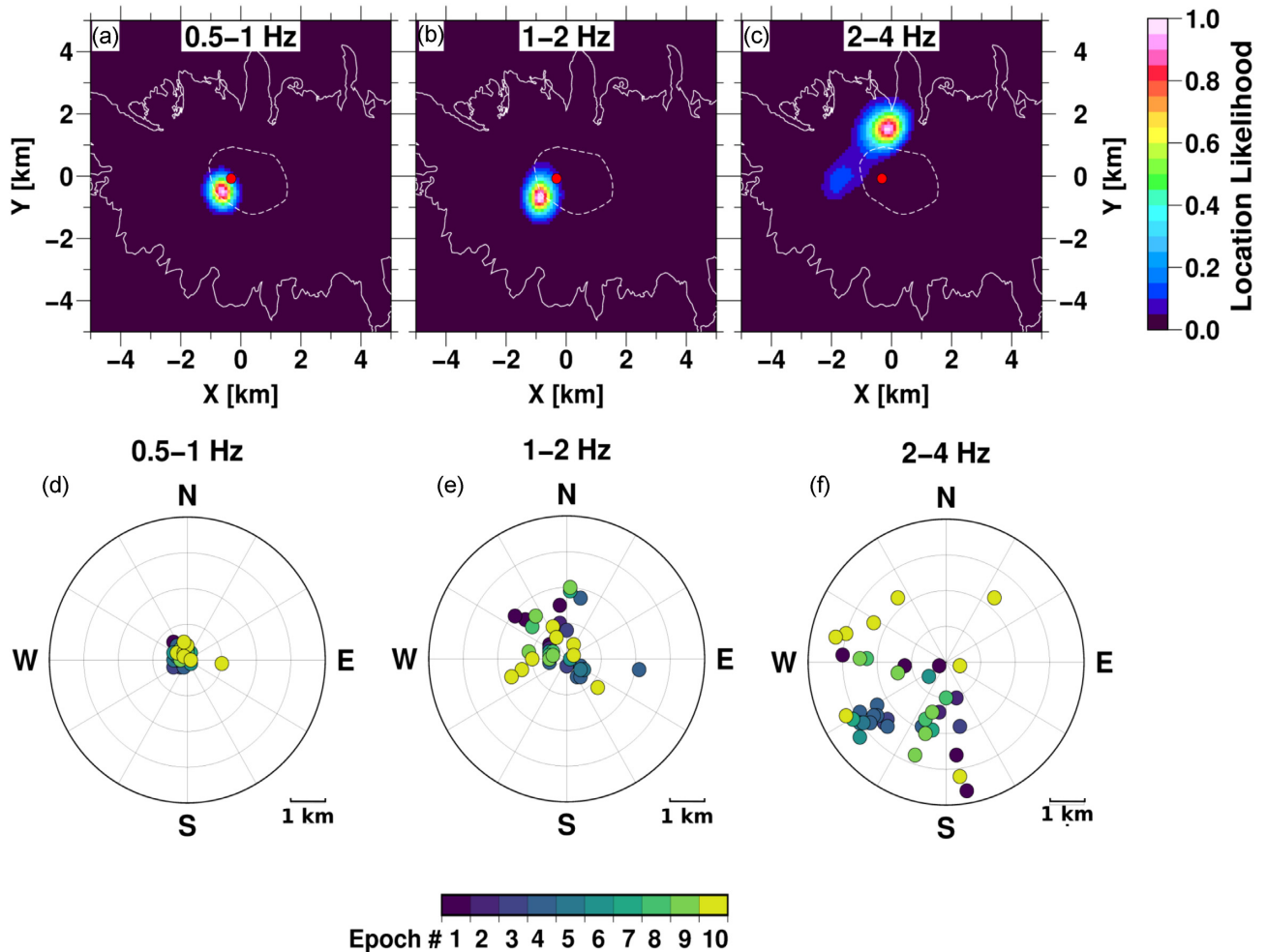
Figure 7. Location likelihood and its stability. Panels (a, b, c) show the location likelihood of the tremor source for eruption-long correlograms filtered between 0.5–1 Hz, 1–2 Hz and 2–4 Hz, respectively. White and dashed lines depict the outline and caldera of Eyjafjallajökull, respectively. The red circle shows the eruption site (Gudmundsson *et al.* 2012). The colour palette on the right defines the location likelihood. Panels (d)–(f) show the location of daily peak likelihood for the three frequency intervals, relative to the long-term average location. Red colours denote days near the beginning of the eruption, blue colours denote days at its end according to a subdivision of the eruption history into 10 epoch defined in Section 5. Circular grid lines define 1 km distance increments.

locations and the location in Figs 7(a)–(c) is shown in Figs 7(d) and (e), colour coded with time. The location of the tremor, as predicted by daily cross correlations, varies by less than 1 km in the 0.5–1 Hz frequency range, less than 2 km in the 1–2 Hz frequency range, but by as much as 3–4 km in the 2–4 Hz frequency range. The inferred location is the same in the two lower frequency ranges and very close to the eruption site, while the average location in the highest frequency range is 2 km to the NNE from the main eruption site and outside the caldera.

The width of the likelihood peak is about 0.5 km in the lowest frequency range and 0.7 km in the intermediate range. At the highest frequencies the width approaches 1 km and significant secondary peaks begin to appear. The inferred locations can not be clearly distinguished from the eruption site. The scatter diagrams in Figs 7(d)–(f) suggest that the uncertainty of daily locations is less than 1 km at 0.5–1 Hz, but larger than 1 km at 1–2 Hz. Note how stable the correlograms are in Fig. 6, also suggesting a stability of the tremor location.

The scatter of the daily locations is comparable to the width of the location-likelihood peak in the lowest-frequency range. One clear outlier is present at the end of the eruption in the 0.5–1 Hz frequency

range (Fig. 7d). This relates to the falling levels of power in the tremor at the end of the eruption. In the intermediate-frequency range the scatter is considerably bigger. Some of the outliers of the distribution occur near the beginning of the eruption (red dots), but most of them towards the end (dark blue dots). Many of the daily locations between epochs 3 and 8 lie within 1 km of the average location, which is comparable to the width of the location-likelihood peak of the eruption-long location estimate.

The daily-location scatter is higher yet in the highest-frequency range. The most likely location in this case is about 2 km NNE of the locations in the lower frequency bands. Most of the daily locations fall between W and S of the most likely location. The most likely location over the whole eruption is not a linear combination of the daily locations, which can explain the uneven distribution of the daily locations around the likelihood peak in Fig. 6(c). The scatter to the south and west suggests locations closer to the most likely locations in the two lower frequency bands. One cluster of locations spanning epochs 3–7 is found about 2–3 km SW of the average location. This corresponds to the secondary peak in the likelihood in Fig. 6(c). Daily locations for epoch 10 behave differently, which can be attributed to declining power in the eruption. We cannot

discuss the uncertainties of these locations with confidence. It is likely that a scaling of a factor of two is conservative for these frequencies due to a more vigorous scattering process at the higher frequencies.

We applied the Li & Gudmundsson (2020) method to surface waves in two dimensions. Consequently, we cannot say much about depth. With better station density, good enough traveltime information, and sufficient body-wave content in the tremor the method could potentially be applied to body waves in three dimensions. This might provide useful constraints on the depth of the source of the tremor. We were not able to do that with the data here. We can, however, say something about the depth based on the excitation efficiency of surface waves. At 1 Hz and with a phase velocity of approximately 1.5 km s^{-1} (somewhat higher than the group velocity) the wavelength will be 1.5 km. Eigenfunctions of fundamental-mode surface waves with that wavelength have energy concentrated in the top 0.5–1 km [extrapolating eigenfunctions from Benediktsdóttir *et al.* (2017) and Jeddi *et al.* (2017)]. Thus, if these surface waves are fundamental mode, they are most effectively excited quite near the surface, that is approximately within he top kilometre. Note, that if the source is at depth in a layered structure, that would cause a common phase shift to the surface waves at two stations, which would cancel in the correlation.

In conclusion, we argue, based on the stability of correlograms between 0.5 and 2 Hz over time, and the narrowness and stability of the location likelihood over time that the tremor source at these frequencies is very localized and stable in location over the entire 5–6 weeks of the eruption. The map location of the source cannot be distinguished from the eruption site (Fig. 7a). The source of the surface waves in the tremor most likely lies within the top kilometre of the volcano.

6 ANALYSES OF POWER VARIATIONS

The stability of the source location allows for a simplification in the analysis of the amplitude or power behaviour with distance.

The decay of the amplitude of a wave with distance, r, can be described as

$$A = A_0 g(r) s(r), \tag{1}$$

where A_0 represents the source strength, $g(r)$ is a geometrical spreading function and $s(r)$ describes attenuation (e.g. Battaglia & Aki 2003; Battaglia *et al.* 2005). For a homogeneous medium (velocity), the effect of geometrical spreading is given by

$$g(r) = r^{-a}, \tag{2}$$

where the exponent is $a = 1$ for body waves and $a = 0.5$ for surface waves. The uniform attenuation factor is given by

$$s(r) = \exp\left(\frac{-\pi f r}{Q v}\right), \tag{3}$$

where Q is an attenuation quality factor, v is the velocity of the wave, r is distance from the source and f is frequency.

When velocity and attenuation are not uniform the factors $g(r)$ and $s(r)$ become path or station dependent. For the ith station we write

$$g_i = \gamma_i r_i^{-a} \tag{4}$$

introducing a station amplitude correction γ_i. The attenuation term becomes

$$s_i = \exp\left(-\pi f \int_{\text{path}_i} \frac{\mathrm{d}r}{Q v}\right) = \exp(-\pi f q_i), \tag{5}$$

where

$$q_i = \int_{\text{path}_i} \frac{\mathrm{d}r}{Q v}. \tag{6}$$

This simple formulation has been commonly used in analyses of tremor amplitude (e.g Battaglia & Aki 2003; Battaglia *et al.* 2005).

In the presence of noise, $n(t)$, the amplitude recorded at the ith station can then be described with

$$A_i(t) = h_i A_0(t) + n_i(t), \tag{7}$$

where $h_i = g_i s_i$ describes a decay factor incorporating both geometrical spreading and attenuation along the path from the tremor source to the ith station. This factor depends on the properties of the path between the receiver and the source. If the source is stationary, then the path between the receiver and the source remains unchanged with time and this station dependent amplitude coefficient also remains unchanged.

In Section 5.1 we showed that the map location of the tremor source was stationary during the entire duration of the eruption for frequency intervals 0.5–1 Hz and 1–2 Hz. If the noise source is also stationary in time and if the tremor source and the noise source are independent with zero mean, then

$$p_i(t) = h_i^2 p_0(t) + m_i(t), \tag{8}$$

where p_i, p_0 and m_i are the power of the time series recorded at station i, the tremor source, and the background noise at station i, respectively. The same formulation is used for a reference station, $i = r$,

$$p_r(t) = h_r^2 p_0(t) + m_r(t). \tag{9}$$

Combining the two power equations we get

$$p_i(t) = \frac{h_i^2}{h_r^2} p_r(t) + m_i(t) - \frac{h_i^2}{h_r^2} m_r(t). \tag{10}$$

Thus, if the noise process is stationary in time, and we plot the power at the ith station against the reference station, we should get a straight line with slope

$$\alpha_i = \frac{h_i^2}{h_r^2} \tag{11}$$

and intercept

$$\beta_i = m_i - \frac{h_i^2}{h_r^2} m_r. \tag{12}$$

With the above description the slope of this line will be unchanged with time if the source location is stationary and the velocity and attenuation in the medium do not change significantly. We have plotted the power-spectral density for each station versus that of a reference station within the two frequency ranges that resulted in a stable location using the probabilistic inference method. We use station fag for reference because it lies closest to the source and has the least disrupted recording throughout the eruption. Examples of results are presented in Fig. 8 and a full range of similar figures for all components are in Appendix A2.

Before calculating the power-spectral density we clipped earthquakes that exceed the continuous tremor in amplitude by calculating the standard deviation of the time-series over hour-long windows and setting values larger than 2 standard deviation to that value. This was then iterated several times. The power-spectral density was calculated within three hour windows throughout the eruption period (Fig. 8). Station fag is 7 km from the eruption site, station bas 10 km and station god 17 km (Figs 1 and 2). The temporal variation of the
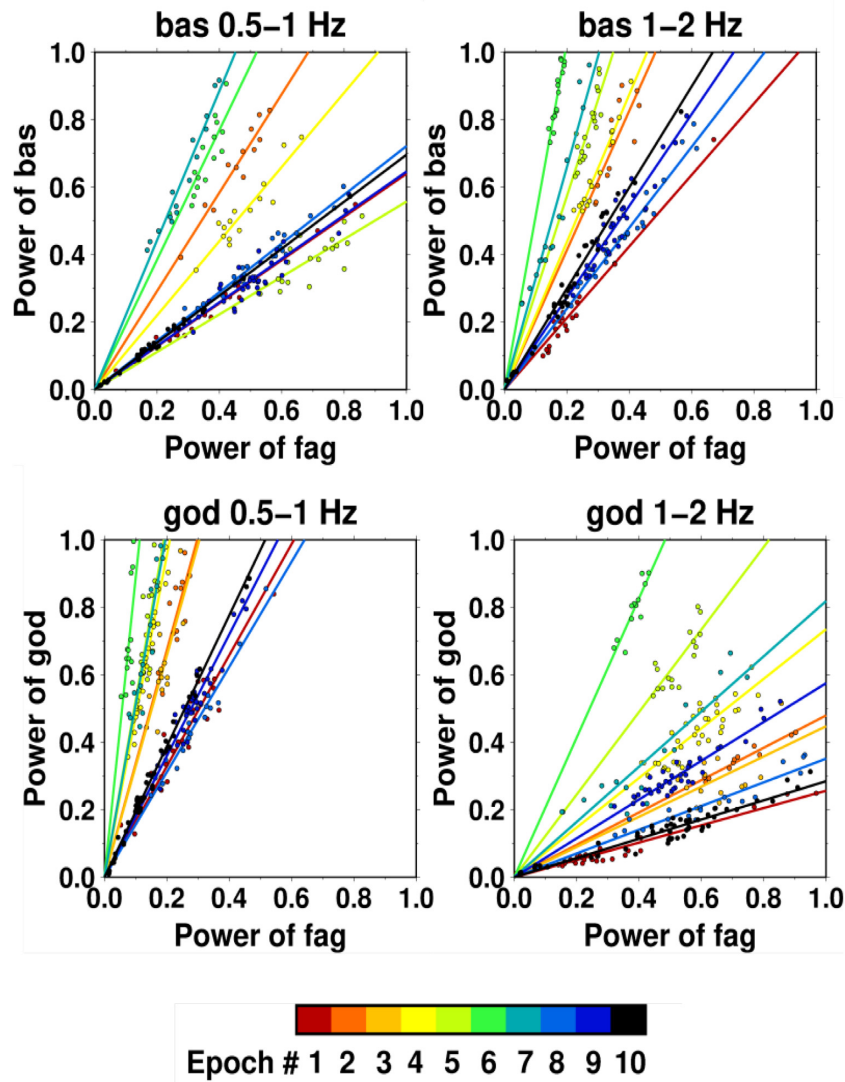
Figure 8. Power of stations bas and god versus station fag during the entire eruption of Eyjafjallajökull, filtered in two frequency bands. Colour code is by epochs of the eruption (see Table 3). Each point on the plot is the mean power calculated over 3 hr.

Table 3. Epochs of the Eyjafjallajökull eruption as defined by the power-ratios analyses.

Epoch #	Duration
1	14th−18th April
2	18th−20th April
3	20th−23rd April
4	23rd−29th April
5	29th−2nd April
6	2nd−4th May
7	4th−6th May
8	6th−9th May
9	9th−14th May
10	14th−21st May

ratio between the stations' power clearly arranges itself into time periods when the slope is relatively stable, while it changes significantly from one period to the next. This leads us to define 10 epochs (Table 3) spanning the eruption during each of which the power ratio is apparently constant, and measure the slopes in each case by linear regression. Each measurement of slope is associated with an uncertainty estimate based on the scatter around the best line in each case. If the uncertainty of the slope exceeded 30 per cent of its value, that measurement was not considered. Also, 10 or more points were required to define a line.

The slopes become progressively smaller with increasing frequency at station god which is a clear attenuation effect. The slopes are high (>1) for station god despite the fact that it is about twice as far away from the eruption site than station fag suggesting significant site amplification at station god. The same does not hold for station bas as the difference in distance is small and the differential attenuation between stations bas and fag is in fact negative as will become apparent later.

From these observations we can extract information about the attenuation quality factor. We also must introduce some aspect of the source that varies with time to produce varying slopes. We will come back to this point later where we propose that the power-radiation pattern of the source may have changed with time.
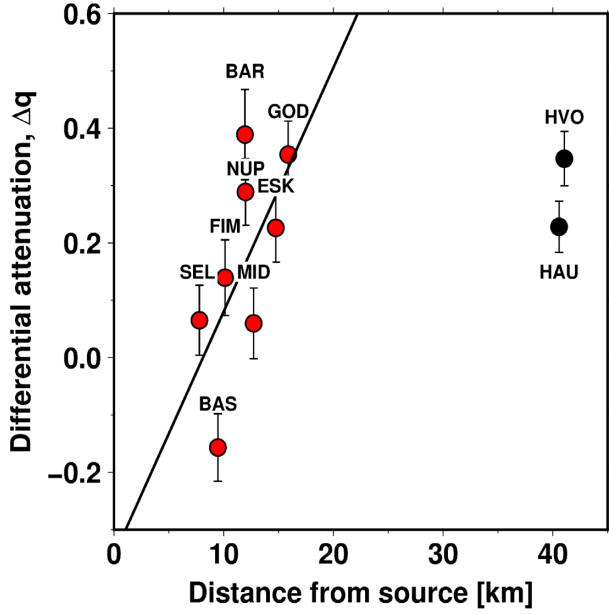
Figure 9. Differential quality factors as a function of distance from the eruption site. Data for all stations (red circles) except hau and hvo (black circles) lie on a line with a slope 0.042 and intercept with the *y*-axis at –0.33. Numerical values for the differential attenuation parameters ($q_r - q_i$) and inferred path-averaged attenuation parameters (Q) to individual stations are listed in Table 5.

6.1 Estimates of attenuation

Concentrating on the attenuation effect, we can write the amplitude factor at the *i*th station as

$$h_i = g_i \exp(-\pi f q_i). \tag{13}$$

Inserting eq. (13) into eq. (10) for the slopes in Fig. 8 and taking the logarithm we get

$$\ln(\alpha_i) = 2(\ln(h_i) - \ln(h_r)) = 2(\ln(g_i) - \ln(g_r)) + 2\pi f(q_r - q_i). \tag{14}$$

Calculating the difference between the natural logarithm of measured slopes at different frequencies during the same epoch at the same station we get

$$\ln(\alpha_i(f_1)) - \ln(\alpha_i(f_2)) = 2\pi(f_1 - f_2)(q_r - q_i). \tag{15}$$

This assumes that a, γ_i and Q are not frequency dependent. We can now estimate the difference $\Delta q = q_r - q_i$, that is a measure of differential attenuation between two paths. We use only the two lowest frequency ranges to do this as we are not confident that the source location is stationary in time for the third and highest frequency range. We simply take the mean frequency of each frequency range as our measure of frequency. For each station we have several measurements of the differential attenuation, one measurement for each epoch if there was data available. Their average (weighted) is our measure of differential attenuation and their scatter defines their uncertainty. The results are shown in Fig. 9 as a function of the distance to the eruption site of the *i*th station in each case. The stations define two groups. The stations close to the eruption site, that is stations around the periphery of Eyjafjallajökull (red), fall close to a line, while the distal stations hvo and hau (black) fall off the line. This suggests that this measure of attenuation is a linear function of horizontal distance from the eruption site within the volcano, that is that the attenuation quality factor, Q, is more or less constant.

Table 4. Regression parameters for attenuation.

	Z	T	R
Slope	0.043 ± 0.022	0.078 ± 0.014	0.067 ± 0.012
Intercept	-0.34 ± 0.26	-0.79 ± 0.17	-0.60 ± 0.15
Q from slope	16 ± 8	9 ± 2	10 ± 2

Assuming this, the slope of the line in Fig. 9 is a measure of Q inside the volcano and its intercept is a measure of the attenuation along the path to station fag. The regression parameters are shown in Table 4. Assuming a uniform phase velocity of $v = 1.5$ km s^{-1} we find a quality factor of $Q = 16 \pm 8$ for the volcanic region and from the intercept we get $Q_{\text{fag}} = 12 \pm 9$. Using this value for Q_{fag} we can calculate a path averaged Q for the distal stations to be $Q_{\text{hau}} = 39 \pm 15$ and $Q_{\text{hvo}} = 48 \pm 22$. Individual Q values were evaluated using the same calculation and the results are shown in Table 5. Q values for paths within the volcano are relatively low (high attenuation) but reasonable, nevertheless, in comparison with estimates in a similar frequency range at other volcanoes (e.g. Gudmundsson *et al.* 2004; Del Pezzo *et al.* 2006; Kumagai *et al.* 2018; and references therein). These Q values are also similar to those estimated by Gudmundsson & Brandsdóttir (2010) at Hengill volcano in SW Iceland and those proposed by Jeddi *et al.* (2016, 2017) in order to reconcile unrealistic Vp/Vs values inferred by comparing Vp from body waves to Vs from lower-frequency surface waves around nearby Katla volcano.

We note that the lowest point in Fig. 9 represents station bas. The differential attenuation is negative despite the fact that station bas is further away from the eruption site than station fag. This was evident from the slope analyses (Fig. 8) where the slope of the power ratios for station bas increased with increasing frequency, opposite to the character of other stations (Fig. A7). This is also observed for the two horizontal components of bas (Figs A8 and A9). We conclude that the attenuation along the path from the source to station bas is low and when Q_{bas} is calculated directly from the Q value for fag (from the intercept) the result is $Q = 34 \pm 47$, which is substantially, but not significantly higher than the average, $Q = 16 \pm 8$, for paths within the volcano.

The lateral source location is uncertain to within a kilometre for the lowest frequency band. Topography has a lesser effect on the lateral error of the source as does the unknown depth to the source. We argue that the tremor consist mainly of surface waves and the depth to the source is therefore much smaller than the lateral distance.

The same analysis was carried out for the radial and transverse components, rotated according to the direct (straight) path between the station and the eruptive site (Figs A10 and A11). In the volcanic region we find a quality factor of $Q = 10 \pm 2$ and $Q = 9 \pm 2$ for the radial and transverse components, respectively. Results for individual Q values for the horizontal components are shown in Table 5.

6.2 Estimates of geometrical spreading factors

We can now use the estimates of attenuation and estimate the geometrical spreading factors, a and station corrections, γ_i,

$$\lambda_i = \ln(\alpha_i) - 2\pi f(\hat{q}_r - \hat{q}_i) = 2(\ln(g_i) - \ln(g_r))$$
$$= 2(\ln(\gamma_i) - \ln(\gamma_r)) - a(\ln(r_i) - \ln(r_r)). \tag{16}$$

We have multiple redundant data to estimate these. However, the equations are not all independent. Obviously, the geometrical spreading exponent, a, cannot be determined with independent

Table 5. Attenuation parameters evaluated for each station–source path.

Station	$q_r - q_i$			Q		
	Z	T	R	Z	T	R
bas	-0.16 ± 0.06	-0.23 ± 0.16	-0.10 ± 0.11	34 ± 47	11 ± 5	13 ± 5
bar	0.39 ± 0.08	0.24 ± 0.21	0.13 ± 0.16	11 ± 4	8 ± 2	10 ± 3
esk	0.23 ± 0.06	0.32 ± 0.13	0.35 ± 0.10	17 ± 8	9 ± 2	10 ± 2
fag	–	–	–	12 ± 9	5 ± 1	6 ± 2
fim	0.14 ± 0.07	0.08 ± 0.15	0.16 ± 0.10	14 ± 8	8 ± 2	9 ± 2
god	0.35 ± 0.06	0.42 ± 0.14	0.45 ± 0.10	15 ± 6	9 ± 2	10 ± 2
hau	0.23 ± 0.04	-0.09 ± 0.21	0.08 ± 0.09	39 ± 15	22 ± 3	24 ± 4
hvo	0.35 ± 0.05	0.46 ± 0.10	0.51 ± 0.07	48 ± 22	39 ± 15	40 ± 10
mid	0.06 ± 0.06	0.22 ± 0.15	0.29 ± 0.11	21 ± 14	9 ± 2	10 ± 2
nup	0.29 ± 0.06	0.23 ± 0.14	0.34 ± 0.12	13 ± 5	8 ± 2	8 ± 2
sel	0.07 ± 0.06	-0.18 ± 0.14	-0.08 ± 0.09	13 ± 8	9 ± 3	10 ± 3

station corrections. A common strategy is to use regional events (Battaglia & Aki 2003) to estimate the station corrections, γ_i. This is not obviously appropriate. As these station-amplitude corrections must include both focusing or defocusing effects along each path and site amplification. Therefore, the geometry of the calibrating wave must be the same as that of the tremor waves. The radiation pattern of the event must also be similar to that of the tremor and the correction needs to be evaluated at the same frequency as the tremor. Calibration with a single phase from a regional event will include effects of energy transfer (in time) in the seismogram by scattering which may differ from the power-spectral density of the tremor. We looked for regional events in the vicinity of the eruption site with sufficiently high signal-to-noise ratio in the frequency range of the analysed tremor and found none. We are, therefore, left with no means of estimating geometrical spreading parameters other than from our tremor-power observations. We do this by applying Occam's razor. We estimate the geometrical spreading exponent, a, so as to minimize the quadratic size of the station correction terms, $\ln(\gamma_i)$. This yields the simplest possible parameter model in just that sense. To do this, we set up a quadratic regression for the station corrections using the linear expression in eq. (16) in terms of reduced (by attenuation) logarithmic station corrections, λ_i, fixing a. Then, we estimated a so that the quadratic sum of the correction terms was minimized. This is a straight forward least-squares problem. We have ten stations, that is 10 unknown differential station corrections, $\ln(\gamma_i) - \ln(\gamma_r)$. We have 160 reduced measures of logarithmic slopes, λ_i, that is a highly redundant problem. We add one constraint, namely that the logarithmic station corrections are evenly distributed around zero (i.e. the station corrections themselves are evenly distributed around unity according to logarithmic distance). We find $a = 0.53 \pm 0.05$ using a jack-knife approach to estimate the uncertainty. This value is very close to the theoretical value for surface waves emanating from a point source. Thus, the power-spectral decay with distance suggests that the tremor at the analysed frequency band consists mostly of surface waves. Therefore, we simply fix $a = 0.5$ and compute the station corrections accordingly. The results are shown in Fig. 10 and Table 6 in terms of their azimuthal and distance variation.

Most of the relative station corrections lie in the range 0.7–2. They do not exhibit any simple azimuthal pattern. Neither is there a systematic behaviour with distance. Station god sticks out with its high value (5.3). It is at 1200 m above sea level in the highland region called Godaland. The site is close to the edge of the highland facing Eyjafjallajökull rising some 1000 m above its surroundings and with a very rugged outline eroded by small outlet glaciers from Mýrdalsjökull that cover Katla volcano to the east. It is conceivable that this rather extreme topography cause significant site amplification for waves from the west.

6.3 Residual analyses

Having estimated a and the γ_i we can reduce our measured slopes or power ratios. According to our above description of amplitude and power the residuals should be

$$d\lambda_i = \lambda_i - 2(\ln(\hat{\gamma}_i) - \ln(\hat{\gamma}_r) + 2\hat{a}(\ln(r_i) - \ln(r_r)) = 0, \qquad (17)$$

that is trivial. But, the quadratic norm of these residuals normalized by the remaining number of degrees of freedom was on the order of $6 \gg 1$. This model of attenuation and spreading does not account for the observed variability and is, therefore, missing something. The residuals still contain information about the variable power ratios with time, a temporal variation that has not been accounted for. We argue that it can be accounted for by adding a temporal variation to power radiation. This can be done by adding a temporal term in the description of the source term in eq. (7).

$$A_i(t) = h_i A_0(t) B(\phi, t) + n_i(t), \qquad (18)$$

where ϕ stands for azimuth from the source and the added term, $B(\phi, t)$, represents relative amplitude-radiation variations with azimuth, ϕ, and time. B does not vary within each epoch. We can therefore absorb the temporal variation of B in its epoch index, k, that is $B_i^k = B(\phi_i, t_k)$. The logarithm of measured power-spectral ratios would then be described as

$$\ln\left(\alpha_i^k\right) = 2\ln\left(\frac{\gamma_i}{\gamma_r}\right) - 2a\ln\left(\frac{r_i}{r_r}\right) - 2\pi f\left(q_i - q_r\right) + 2\ln\left(\frac{B_i^k}{B_r^k}\right) \qquad (19)$$

and the residuals after correction for attenuation and geometrical spreading become

$$d\lambda_i = \lambda_i - 2(\ln(\hat{\gamma}_i) - \ln(\hat{\gamma}_r) + 2\hat{a}(\ln(r_i) - \ln(r_r))) = \ln\left(\frac{C_i^k}{C_r^k}\right), \qquad (20)$$

where $C_i^k = \left(B_i^k\right)^2$, that is the relative power radiation. We now have a relation to estimate the variable relative power-radiation pattern at each station for each epoch. In eq. (20), we have assumed that the power-radiation patterns do not depend on frequency. But, we need not do that as we can group our residual measurements within each frequency range. This, however, involves no redundancy. Such estimated relative power-radiation patterns, C_i^k/C_r^k, are shown in the left and middle columns of Fig. 11 for the 0.5–1 Hz and 1–2 Hz frequency ranges, respectively. The right column of Fig. 11 shows
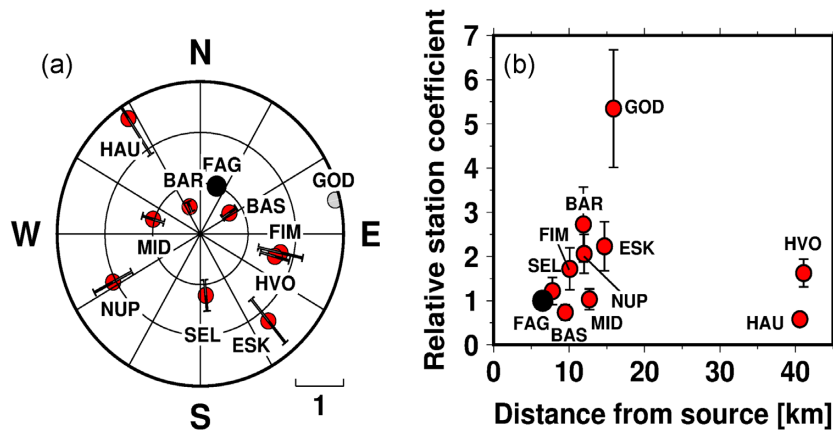
Figure 10. Estimates of relative station coefficients for each station (γ_i/γ_r) in a rose diagram (a) and as a function of distance from eruption site (b). Black point represents the reference station *fag*. The grey point for station god plots off scale in (a). Numerical values of the logarithm of the relative station correction parameters and the inferred station correction parameters themselves are displayed in Table 6.

Table 6. Station correction parameters evaluated for each station-source path.

Station	$\ln(\gamma_i/\gamma_r)$			γ_i		
	Z	T	R	Z	T	R
bas	-0.31 ± 0.24	-0.30 ± 0.69	0.17 ± 0.42	0.48 ± 0.12	0.62 ± 0.43	0.72 ± 0.30
bar	1.00 ± 0.32	0.17 ± 0.79	0.06 ± 0.50	1.78 ± 0.56	0.99 ± 0.78	0.65 ± 0.32
esk	0.80 ± 0.25	0.59 ± 0.52	0.78 ± 0.44	1.46 ± 0.37	1.50 ± 0.78	1.33 ± 0.53
fag	–	–	–	0.65 ± 0.50	0.83 ± 1.59	0.61 ± 0.74
fim	0.54 ± 0.28	0.00 ± 0.61	0.42 ± 0.36	1.13 ± 0.32	0.83 ± 0.51	0.93 ± 0.34
god	1.68 ± 0.25	1.59 ± 0.58	1.90 ± 0.38	3.53 ± 0.88	4.08 ± 2.36	4.09 ± 1.5
hau	-0.54 ± 0.18	-1.55 ± 0.74	-0.92 ± 0.32	0.38 ± 0.07	0.18 ± 0.13	0.24 ± 0.08
hvo	0.48 ± 0.19	1.28 ± 0.37	1.32 ± 0.27	1.06 ± 0.20	2.99 ± 1.10	2.29 ± 0.62
mid	0.03 ± 0.23	0.45 ± 0.58	0.68 ± 0.37	0.68 ± 0.16	1.30 ± 0.76	1.21 ± 0.45
nup	0.72 ± 0.21	0.39 ± 0.52	0.97 ± 0.42	1.35 ± 0.18	1.23 ± 0.64	1.61 ± 0.68
sel	0.20 ± 0.25	-0.59 ± 0.53	0.03 ± 0.34	0.80 ± 0.20	0.46 ± 0.24	0.63 ± 0.21

the weighted average of the other two with weight inversely proportional to the error estimate in each case. The reference station, *fag*, is shown as a black circle, located 55° east of north. Relative power-radiation patterns for the horizontal components are shown in Figs A14 and A15.

It is important to note that the definition of the ten different epochs was exclusively based on the tremor data, that is independent of any other data. Fig. 6 shows how the ten epochs, defined here, and the four intervals of Gudmundsson *et al.* (2012) compare.

The resulting power-radiation patterns relative to station *fag* (Fig. 11) generally show a marginally significant difference between the two analysed frequency bands (with several exceptions, for example station hau in epoch 2 and station hvo in epoch 6). In some cases, the estimated patterns differ significantly from one epoch to another, for example epochs 7 and 8, but in others the epochs are almost the same, for example epochs 8, 9 and 10. Some apparent inconsistencies are present and station hvo sticks out in that regard. Stations hvo and fim are at very similar easterly azimuth and are not always comparable.

Epochs 1, 8, 9 and 10 exhibit a nearly isotropic power-radiation pattern. These epochs are synchronous to phases I, III and IV, where the tremor had lower amplitudes and the activity was primarily explosive. It is mainly within phase II (epochs 2–7) that there is variation in the power-radiation pattern. Phase II was the only phase that included effusive eruption. Perhaps the explosive source is most isotropic and the effusive part is more dependent on the orientation of the fissure/cauldron making it non-isotropic. Some of the epochs

are poorly defined, because of lack of data (e.g. epoch 3) while others show a wide scatter of points with large error bars (e.g. epochs 2 and 6).

6.3.1 Addendum

In the appendix, we present results of parameter estimation based on the horizontal components of data. We note that the time behaviour of power is similar on all components on all stations. The power ratio between the horizontal components and the vertical component is consistently on the order of 1 (varies in general between 0.3 and 1.7). In the linear regression for power-spectral ratios the slope is the datum we seek, but the intercept is an indicator of power in the noise process in each case. We find that the intercepts range from equal to higher by up to a factor of 10 on the horizontal components than on the vertical. This indicates that the noise on the horizontal components is often higher than that on the vertical. We rotated the horizontal components into the radial and transverse for each path from the inferred source location. From the horizontal components (R and T) we estimate parameters that are quite similar to those determined from the vertical component (Z).

The path-averaged attenuation coefficients are estimated to be $Q = 10 \pm 2$ and 9 ± 2 for the volcanic region and $Q_{\text{fag}} = 6 \pm 2$ and 5 ± 1 from the R and T components, respectively, as opposed to $Q = 16 \pm 8$ and $Q_{\text{fag}} = 12 \pm 9$ from the Z component. For the distal stations, hau and hvo, we estimate a path averaged Q to be $Q_{\text{hau}} = 24 \pm 4$ and 22 ± 3 and $Q_{\text{hvo}} = 40 \pm 10$ and 39 ± 15, for
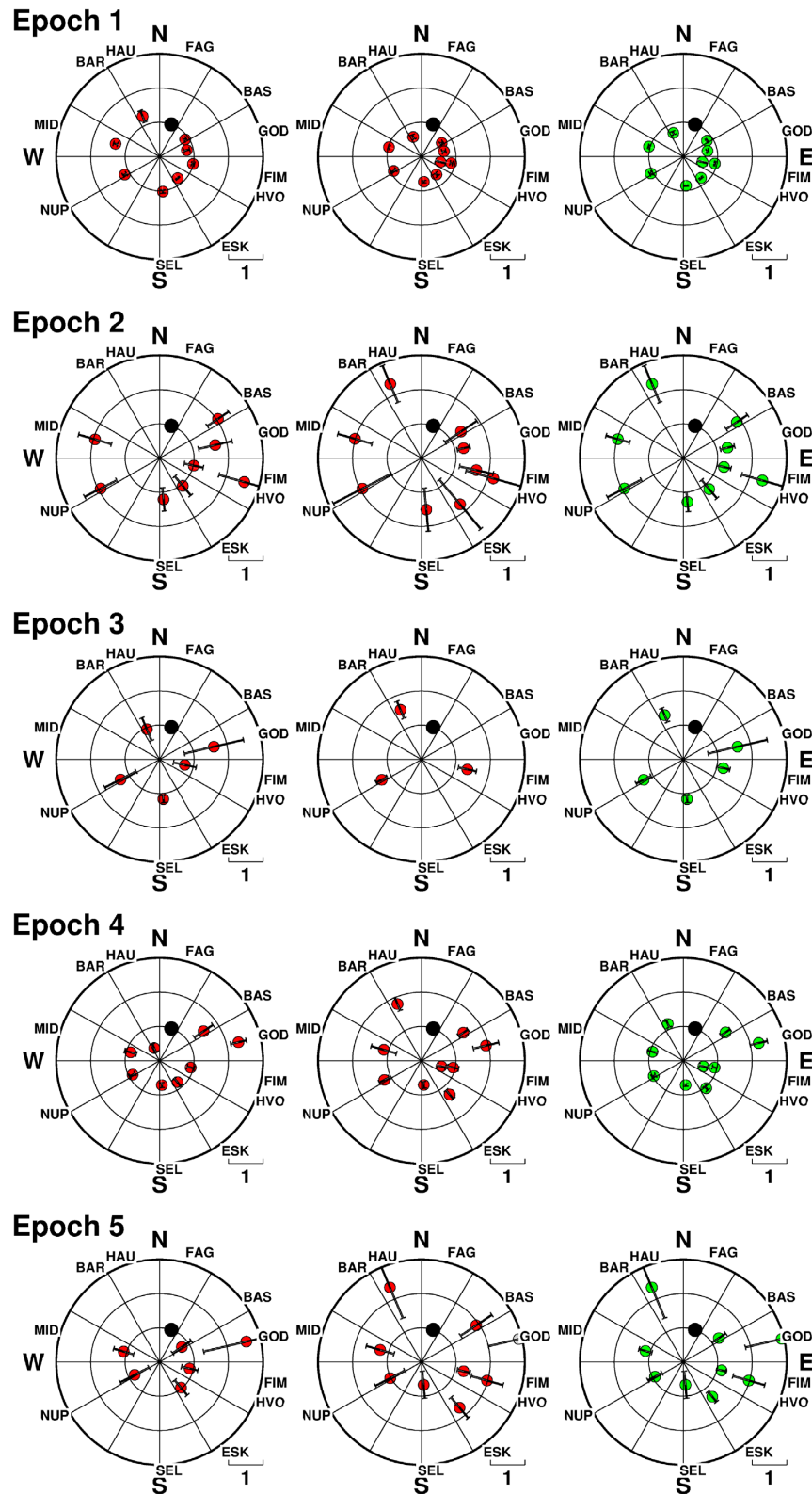
Figure 11. Estimates of the power-radiation pattern relative to station *fag* for 0.5–1 Hz (left-hand panel), 1–2 Hz (middle panel), and a weighted mean of the two frequency intervals (right-hand panel). Where only one measurement was available for one frequency interval, that value was taken as the weighted mean. The error bars are the estimated errors of power-spectral ratios (slope). *fag* is plotted as a larger black circle without an error bar.
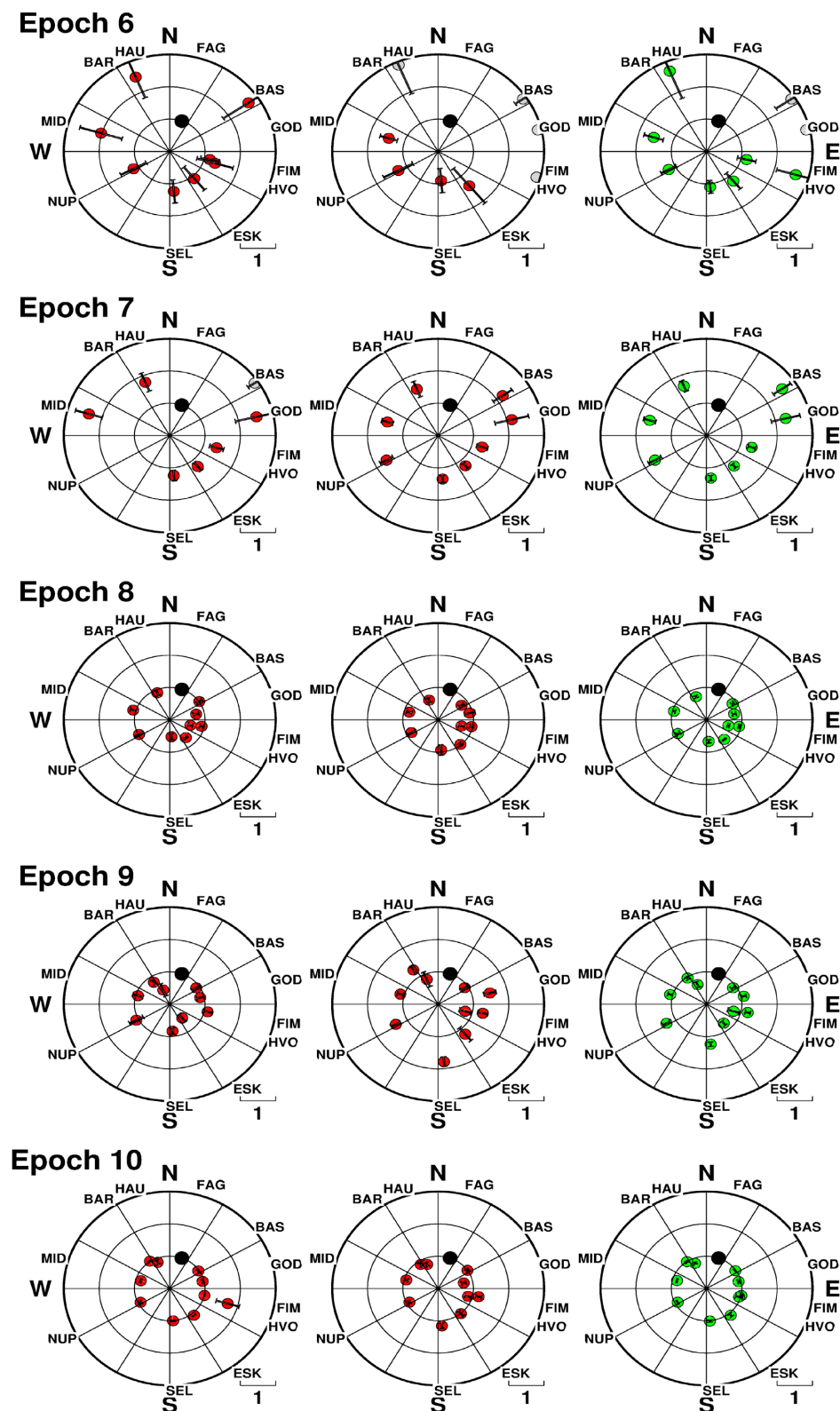
Figure 11. *continued*

the *R* and *T* components, respectively. The *Q* estimates from the horizontal components are comparable, but somewhat lower than the estimates based on the *Z*-component. This may indicate that the attenuation of Love waves is greater than for Rayleigh waves. Figs A11 and A10 show the differential quality factor for the *R* and *T* components as a function of horizontal distance from the eruption site. Numerical values for the differential attenuation parameters ($q_i - q_r$) and the attenuation parameters (*Q*) are displayed in Table 5.

Estimates of station corrections are also similar based on the horizontal components as those based on the vertical component.

The two stations that stick out are station god and hvo with a high relative station correction ($\approx 3-4$). The estimated relative radiation patterns are also similar (Figs A14 and A15). We refer the reader to Figs A12 and A13 and Table 6 for numerical values of the station correction parameters for the horizontal components.

7 DISCUSSION

We have measured the time-space variation of tremor associated with the 2010 Eyjafjallajökull summit eruption based on differential-phase information. In the following, we discuss the spatial and amplitude variation of this tremor and our results in a wider context.

The beginning of the 2010 Eyjafjallajökull is similar to the prelude to eruption at other volcanoes in Iceland, that is Krafla (Brandsdóttir & Einarsson 1992), Grímsvötn (Vogfjörd *et al.* 2005) and Bárdarbunga (Einarsson & Brandsdóttir 1984; Eibl *et al.* 2017b). An intense and short microearthquake precursory volcano-tectonic swarm (Tarasewicz *et al.* 2012a) is accompanied by increased tremor levels at a wide range of frequencies that precedes steady eruption tremor at lower frequencies (0.5–10 Hz).

The tremor, was strictly associated with the Eyjafjallajökull eruption itself; it began when the eruption started and faded out in the eruption's waning stages. This behaviour is similar to other volcanoes, for example tremor associated with the unrest at Katla volcano in 2011 (Sgattoni *et al.* 2017), tremor associated with the Holuhraun eruption in 2014 (Eibl *et al.* 2017a), tremor during the Grímsvötn eruption in 2004 (Vogfjörd *et al.* 2005) and tremor observed during the Krafla Fires (Brandsdóttir & Einarsson 1992).Tremor was continuous in time with varying amplitude, distributed in frequency between about 0.5 Hz and 5 or 10 Hz, depending on station distance and eruptive character (Fig. 2).

7.1 Tremor during the beginning of the eruption

According to Magnússon *et al.* (2012) the first flood was observed to propagate from the lagoon north of Gígjökull into the glacial river at 8:27 on 14 April, which coincides with the onset of the first tremor peak (T1) and matches a rapid increase of the water level at the gauge in front of Gígjökull (Fig. 4d). Therefore, the time lag between the onset of the tremor and the onset of the flow peaks at Markarfljót could correspond to the time it takes the jökulhlaup to reach Markarfljót.

The time-lags between the tremor peaks and the flood peaks at Markarfljót were 2 hr and 50 min, 3 hr and 30 min and 4 hr for the four flood peaks, T1, T2 and T4.

Assuming that the flood-water went down Gígjökull and then to the gauge at Markarfljót, the distance is roughly 20 km. The subglacial flood path was less than 5 km, which leaves 15 km for the subaerial part of the flood. Eibl *et al.* (2020) reported the subaerial speeds of the flood to be 10 km hr^{-1}. Assuming similar rates in the case of the Eyjafjallajökull jökulhlaups, we get subglacial flood speeds of 3.75, 2.5 and 2.0 km hr^{-1} for the flood peaks T1, T2 and T4. Eibl *et al.* (2020) reported subglacial flood speeds of $1.4-2.4$ km hr^{-1} for floods with a peak discharge of 3000 m^3 s^{-1} and flood speeds in the range of $0.7-1.6$ km hr^{-1} for floods with a peak discharge of $210-380$ m^3 s^{-1}. The peak discharge for flood peaks T1, T2 and T4 was 2500, 700 and 1200 m^3 s^{-1}, respectively. The rates for the subglacial floods associated with the 2010 Eyjafjallajökull eruption are therefore comparable to those reported in Eibl *et al.* (2020).

The flood peaks observed at Markarfljót were not seen in the tremor data at nearby station mid. The tremor peaks start at the same time at all stations. Therefore, recorded tremor must be dominated by processes near the common eruption source or by subglacial floods. If the tremor were associated with the subaerial flood, it would have been recorded at station mid and even some other nearby station, starting at different times with the progression of the flood.

Fig. 5(b) shows the tremor episode in tremor peak T3. Periodic tremor peaks occur prior to the main burst, roughly every 12 min. Much of the energy is focused at 0.8, 1.4 and 2.4 Hz, although it is distributed between 0.4 Hz and up to more than 10 Hz. The peaks start with a small amplitude that increases until approximately 18:20 when a loud roar was heard (Magnússon *et al.* 2012) and the floodwater most likely escaped and rushed down Gígjökull. The flood-peak at Markarfljót associated with T3 arrived 1 hr and 40 min later, at 20:00. Using the subaerial speeds of Eibl *et al.* (2020) of 10 km hr^{-1}, we obtain the subglacial speed of 15 km hr^{-1}. The peak discharge of flood peak T3 was 1100 m^3 s^{-1}. Tremor peak T3 and the flood associated with it are anomolous compared to the other tremor peaks, the tremor had different characteristics (as described above) and the flood speed reported for flood peak T3 is much larger than for the other flood peaks, T1, T2 and T4.

The starting times of the floods are assumed to be at the start of their associated tremor peak. These are assumptions and therefore the flood speed should be taken with care.

7.2 Correlation of tremor and eruption processes

Features of the temporal variation of the tremor amplitude during the summit eruption correlated with the four main phases (see Fig. 1) of the eruption as defined by Gudmundsson *et al.* (2012). During the initial explosive phase (I) tremor intensity varied and included strong tremor bursts that could be associated with subsequent flooding in the lowlands north and west of the volcano (see Figs 3, 4 and 5). It is probable that this phase of the eruption, and the tremor associated with it, was dominated by explosive activity due to the interaction between magma and melt water from the overlying glacier. During the following mixed effusive-explosive phase (II), a 3-km-long lava flow within the caldera drained through its northern rim and explosive activity was relatively weak (Gudmundsson *et al.* 2012). However, the tremor intensity increased and it was redistributed towards higher frequencies (Fig. 3c). This negative correlation between eruptive plume height and tremor intensity can also be found in the tremor variation within this phase of the eruption. Around 26 April the plume height increased from almost zero to approximately 5 km height and a corresponding drop in tremor intensity was observed at station nup (Fig. 3a) and slightly at station fag (Fig. 3b). Also, between 9th and 12th May a decrease in plume altitude was observed and a corresponding increase in tremor levels at both fag and nup (Figs 3a, b and d).

A second explosive phase (III) started on 5th May with ash changing to a slightly more evolved and possibly more volatile-rich (trachytic) composition (Sigmarsson *et al.* 2011). While eruption intensity and plume height increased during this phase, tremor intensity declined slowly but steadily, with little power above 2 Hz (Fig. 2). The negative correlation between plume height and tremor intensity during phases II and III suggests that effusion generates tremor more efficiently than explosive activity near the surface. During the final phase (IV), both eruption and tremor intensity dropped rapidly.

Levels of tremor were lower in amplitude and concentrated at lower frequencies during the explosive phases I and III, compared

to the effusive-explosive phase II (Fig. 3). A similar behaviour, a concentration of the main tremor power at lower frequencies during the explosive phase, has been observed at other volcanoes, for example Mt Etna in Italy (Cannata *et al.* 2008) and during the 1999 eruption of the Shishaldin volcano, Alaska (Thompson *et al.* 2002). Cannata *et al.* (2008) suggested a reduced sound speed of the fluid in the conduit, caused by an increase of the gas-volume fraction, could be the cause of the shift towards lower frequencies. Also, as the explosive activity began, the length of the resonant in the conduit may have increased, thereby causing the tremor to shift towards lower frequencies (Thompson *et al.* 2002).

Eibl *et al.* (2017a) found that the lava fountain height of the main vent correlated with tremor levels, at different times during the 2014–2015 Holuhraun eruption, Iceland. Also, they did not find any correlation between tremor amplitude and effusion rates. In their study, they found three different sources of the tremor, of one was stationary and two were migrating. Perhaps, in their case, multiple synchronous tremor sources are the cause of no link between tremor and fountain height and effusive rate or perhaps the tremor sources were not related to the processes ongoing in the eruptive vents. They also found an increase in tremor levels during the opening of fissures.

In the January–June 2000 eruption of Mt Etna, Alparone *et al.* (2003) found a direct link between tremor levels and fountain height. The eruption took place in the southeast crater of Mt Etna and was characterized by 64 lava fountain episodes. The link between the tremor and fountain episode was so striking that they could predict the next fire-fountain episode with 1–5 hr notice for 86 per cent of the fire-fountain episodes that occurred after 15 May. Relationship with increased fountain height and tremor levels were presented, for two volcanoes (Kilauea, Hawaii and Pavlof, Alaska), in McNutt (1992) where a relationship between increased tremor levels and fountain height was found.

In the March 2016 Pavlof eruption a relationship was found between the tremor levels and the waxing and waning portions of the eruption (Fee *et al.* 2017) with correlation between plume height and tremor levels, which is opposite to the 2010 Eyjafjallajökull eruption. Fee *et al.* (2017) suggested a rapid rise of fresh magma, which decompressed and degassed while ascending, triggering explosive fragmentation. The conduit trewalls and vent were then eroded by a high-velocity flow of particles and gas, producing tremor. In the case of the 2010 Eyjafjallajökull eruption Gudmundsson *et al.* (2012) suggested that a basaltic injection from the mantle into a silicic magma embedded in the crust under the volcano initiated the eruption. The second explosive phase (III), began because of another basaltic injection into the silicic magma in the upper crust (Sigmarsson *et al.* 2011). This interpretation was supported by Tarasewicz *et al.* (2012a) who located earthquakes beneath the brittle–ductile transition zone, that can indicate magma movement.

It is therefore evident that relationships between tremor levels and eruptive character differ from one volcano to another.

7.3 Tremor location

The location likelihood of the tremor using the probabilistic inference method of Li & Gudmundsson (2020) resulted in a very stable location in the 0.5–1 Hz frequency band, a somewhat less stable location in the 1–2 Hz frequency band, and an unstable location in the 2–4 Hz frequency band. The steady reduction of location stability with increasing frequency may be explained by increasing vigour of the scattering suffered by propagating waves from the tremor source

with frequency. The low-frequency tremor (0.5–2 Hz) emanated from a single dominant source, which cannot be distinguished from the main eruption site throughout the course of the eruption. The daily scatter of this location reflects the uncertainty of the location and is less than a kilometre in the lowest frequency range. With a daily resolution, any events with a shorter duration than that cannot be resolved. Other sources at higher frequencies might be possible. In fact, the average tremor location in the frequency range between 2 and 4 Hz is substantially displaced from that of the lower frequencies and lies close to the northern caldera rim where floodwater and lava drained down the Gígjökull glacial stream (see Fig. 7). It is therefore tempting to associate the higher frequencies in the tremor with either flooding or the lava flow. However, due to a high level of scatter in the daily high-frequency locations it is questionable if this displacement of the source is significant, the flooding only occurred in the early stages of the eruption and the effusive activity is concentrated in phase II of the eruption that spans less than half of the eruption's duration.

Eibl *et al.* (2020) observed two types of tremor sources associated with floods originating from the Western and Eastern Skaftá Cauldrons in Vatnajökull, Iceland. They calculated backazimuth and distance from seismic arrays to pinpoint the location of the tremor source. Type 1 tremor initiated with the start of the subglacial flood, its location changed with the progress of the subglacial flood and it was observed prior to the flood emergence from the glacier. Type 1 tremor was characterized by non-harmonic and low-frequency content. Type 2 tremor started after the flood was initiated and the source location was stationary, close to the cauldron from which the flood originated. Type 2 is characterized by harmonic and high-frequency content. The tremor detected during the Eyjafjallajökull eruption could consist of type 2 tremor. We do not detect a migrating source. The cause could be the short subglacial path of the flood, which is approximately 5 km compared to 40 km of the flood path in the study of Eibl *et al.* (2020).

If there are other tremor sources in the two lower frequency bands, 0.5–1 and 1–2 Hz, we do not detect them as the main source is the only one our method detects. Other events during the eruption could cause tremor. These include the jökulhlaups at the beginning of the eruption and lava flows, that became visible on 21st April (Magnússon *et al.* 2012). However, the phase change on April 18 was likely associated with the initiation of the effusive phase with the slow-moving dacitic lava not appearing from underneath the cinder cone until several days later.

Our locations of the tremor bursts in the early stages of the eruption (with a time resolution of one hour in the 0.5–2 Hz frequency range) are similar to the average tremor-source location (see Fig. 7), although they are naturally less precisely due to lesser redundancy in data over a shorter time period. The velocities we used are suitable for surface waves. The tremor associated with the stable source in the study of Eibl *et al.* (2020) was mostly composed of body waves whereas the tremor caused by the migrating flood was composed of surface waves. Although these bursts (see Fig. 4) occur simultaneously with jökulhlaups (Magnússon *et al.* 2012), they cannot be directly related to the migration of the floodwater. The tremor bursts are most likely associated with the opening of a new vent, that is oscillations in magma-gas pressure within the conduit locally melting more glacier ice and generating subsequent floods. It is likely that fluctuations in magmatic/gas pressures in the eruption conduit and/or magma-water interaction within the new vent, generated these relatively short tremor bursts.

We argue that we cannot compare the tremor of the 2010 Eyjafjallajökull to the jökulhlaup from the Skaftá Cauldrons (Eibl *et al.*

2020) because of different sources. The tremor source in this study is associated with an eruptive vent whereas the source in Eibl *et al.* (2020) is associated with the emptying of a subglacial lake within a ice cauldron.

7.4 Analyses of power variation

We have analysed the amplitude behaviour of the recorded tremor with distance and time, by measuring power ratios between each of the recordings and the recording at a reference station. This allows us to separate variation in the tremor from variation in local noise by assuming independence of the tremor and noise signals. This is important as some of the temporarily deployed seismographs were installed in very noisy conditions (in particular station sel that was deployed in the basement of a cowshed and had a constant noise at 5 Hz, see Fig. 2). We find that the power ratios vary significantly (by up to a factor of 7) between the 10 epochs spanning the eruption period (Table 3), while remaining relatively constant within each epoch (see Figs 8, A7, A8 and A9).

Since the tremor-source location at frequencies between 0.5 and 2 Hz is found to be stable with time based on independent data (i.e. phase and not amplitude or power data) we conclude that the observed variation in the power ratios must be due to either changes in the physical properties of the rocks, that waves in the tremor pass through, or changes in the nature of the source. The former must be considered unlikely. It is difficult to envisage changes in relative power by a factor of 7 over time due to path averaged changes of attenuation or spreading of waves from a single, stable source. Therefore, we conclude that some aspect of the tremor-source radiation has changed with time. This could reflect changes in the horizontal radiation pattern of the source, or changes in the depth of the source and in the wave content of the tremor. Since we find that the tremor consists mostly of surface waves at the analysed frequencies we conclude that the observed variation with time of power ratios at all stations is most likely due to changes in the radiation of the source.

Analyses of tremor amplitude often assume isotropic radiation. The argument can be that the diffusive nature of the scattering process will mix any directivity of the source (Morioka *et al.* 2017). Kumagai *et al.* (2010) used an isotropic source and stated that it can be assumed at frequencies above 5 Hz because of path effects caused by scattering of the seismic wave. This appears not to be the case with data in the frequency range 0.5–2 Hz at Eyjafjallajökull and points out the need to consider potential variation of the power radiation when locating tremor based on amplitude.

7.5 Parameter estimation

7.5.1 Quality factor

We estimated a stable epicentre of the tremor source in two independent frequency ranges, 0.5–1 Hz and 1–2 Hz and obtained redundant estimates of logarithmic amplitude decay of the tremor in the same frequency ranges within 10 different epochs of the eruption. Using these data we can estimate the path averaged differential attenuation between the reference station and each of the other seismic stations from which we have observations of tremor power. This, in turn, allows us to estimate path averaged attenuation coefficients for each station. Estimates of path averaged attenuation coefficients range from $Q \approx 10-20$ for some of the shorter paths to $Q \approx 20-50$ for the distal paths based on the vertical component of

motion and somewhat lower based on the horizontal components. These are indications of strong attenuation, but within the range of $Q = 10-100$ found in volcanic regions (see e.g. Kumagai *et al.* 2018; Del Pezzo *et al.* 2006; Gudmundsson *et al.* 2004). The lower estimates based on horizontal components of motion may indicate that both Rayleigh and Love waves are present in the tremor, scattered so that they are mixed between the horizontal components. Also, the lower estimates on the horizontal components may indicate that the quality factor, Q, is lower for Love waves than Rayleigh waves. Similar observations were reported by Bianco *et al.* (1999) at Mt Vesuvius, Italy.

Fee *et al.* (2017) found that conduit walls were eroded during the course of the 2016 eruption at Pavlov Volcano, Alaska. Also, there might be some structural changes within a volcano during an eruption, such as a new dike intrusions. These events may change the Q during the course of an eruption. However, these changes are small-scale compared to the station-to-volcano path lengths. We also note that we have assumed that Q is frequency independent for the span of the two frequency intervals, 0.5–2 Hz. Q is often found to increase with higher frequency (Del Pezzo *et al.* 2006) but the frequency interval we look at in this study is small compared and the changes of Q are likely to be small.

We find that differential attenuation increases approximately linearly with horizontal distance from the tremor source for those of the stations that are in the near vicinity of Eyjafjallajökull volcano (for all stations except hau and hvo). This holds for analyses of all three components of the tremor records (see Figs 9, A10 and A11). That is consistent with tremor primarily composed of surface waves. If the tremor consisted primarily of body waves, then the depth variation of attenuation would control this behaviour with distance. A concentration of attenuation near the surface, which is likely (Kumagai *et al.* 2018), would in that case lead to a reduced rate of increase of differential attenuation with distance, ultimately a weakening, simply because the incidence angles of the body waves near the surface decrease with distance. Therefore, this corroborates that the 2010 Eyjafjallajökull tremor consists mostly of surface waves.

We cannot estimate the contribution of scattering to our measurements of Q without further characterization of the scattering process. We note that our measurements are direct measurements of the frequency derivative of amplitude integrated over long time windows and may, therefore, be more akin to coda Q, Q_C, than measures of Q based on direct waves at the onset of the waveforms. Scattering certainly contributes to our measurements as scattered surface waves have passed along longer paths than the direct waves.

In the 2014 Holuhraun eruption Caudron *et al.* (2018) estimated Q for S waves at distances of up to few tens of kilometres from the source(s) to be about $Q_s = 175$ in a wide frequency range centred on 9 Hz. These results indicate less attenuation than our results. However, they are not comparable for several reasons. The nature of measurement differs: we measure Q based on a frequency difference of amplitude ratios, while they match amplitude ratios. The wave types differ and consequently the geometry of sampling of the crust: we work with what we argue to be surface waves at a relatively high frequency which sample the top 0.5–1.0 km of the crust, while body waves in the study of Caudron *et al.* (2018) dive deeper into the crust. The frequency content differs: we work with lower frequency and Q is often found to increase with frequency (Del Pezzo *et al.* 2006). Finally, we argue that it may not be entirely clear what the Q factors in Caudron *et al.* (2018) represent. They have applied a power-law decay for geometrical spreading, but it is unclear what is the appropriate geometrical spreading rate for the best 1-D velocity model in their area. The site corrections involved

in the method do not strictly depend on amplification effects beneath each site, but rather describe an integral path effect in light of potential velocity and Q heterogeneity and/or anisotropy. Therefore, trade-off may exist between station amplitude corrections, decay rate for geometrical spreading and Q.

7.5.2 Geometric spreading factor

We have also estimated the rate of decay of the tremor with distance due to geometrical spreading based on a power law and frequency-independent station corrections. This parametrization is similar to that commonly used in analysis of tremor amplitudes (e.g. Battaglia & Aki 2003; Battaglia *et al.* 2005), but the analysis is admittedly simplistic. These station corrections should not be seen as corrections for effects of structure beneath each station, but rather as a correction for the entire path between source and station. They can contain frequency-dependent effects of multipathing and scattering, focusing and defocusing along each path, as well as frequency dependent site amplification. Note that, having estimated differential attenuation, we can correct for it, and thus have many redundant measurements of the decay rate of relative power with distance and relative station corrections for each of 10 epochs for which we have data at each of the stations. We have not been able to calibrate the station corrections with independent data as we have not found earthquakes located in the tremor-source region with a useful signal-to-noise ratio in the frequency range of the tremor. We find, upon application of Occam's razor, that is by seeking the power-law exponent that yields the smallest possible variation of station corrections, a power-law exponent of $a \approx 0.5$ (see eq. 2). This is consistent with tremor primarily propagating as surface waves. The station corrections for the vertical component are plotted against azimuth and distance in Fig. 10 (for the horizontal components see Figs A12 and A13). No systematic behaviour is apparent with azimuth. Their behaviour suggests a steady increase with increasing distance for those of the stations that are near Eyjafjallajökull volcano, but not for the distal stations which might indicate a change of the wave content in the tremor with distance. However, that would require an effective decay rate slower than that of surface waves so that the near stations have been overcompensated by the surface wave decay requiring recompensation in the station corrections. Such distance behaviour is neither found in body waves nor near-field displacement terms.

7.5.3 Relative radiation pattern

We have estimated the relative radiation pattern for the span of the eruption (Figs 10, A8 and A9).

Phase I and epoch 1 cover the same time span. Phase II spans epochs 2–6, phase III spans epochs 7–9 and a part of 10 and phase IV spans rest of epoch 10. The relative power-radiation pattern is approximately circular, that is isotropic, in epochs 1, 8, 9 and 10. These epochs cover phases where the activity was explosive (I and III) and when the activity was waning (IV). During phase II, the activity was effusive with low-discharge and the relative power-radiation pattern was highly variable.

We performed the power-analyses using the four phases of Gudmundsson *et al.* (2012) but found that the variation in phases II and III were such, that we had to divide the phases further. This points to some variability in the eruption character during phases II and III that does not affect other eruption characteristics such as plume elevation.

If the source were non-isotropic in the same fashion during the entire time-span of the eruption, then that variation would be accounted for in the station correction parameter. The estimated power-radiation pattern is therefore a measure of the deviation of a mean power-radiation pattern, relative to station *fag*. Therefore, it is not possible to link the pattern in Fig. 11 to an absolute power-radiation pattern.

7.6 Depth estimate

Surface waves around 1 Hz at Eyjafjallajökull have a phase velocity around 1.5 km s^{-1} and a wavelength of about 1.5 km based on extrapolation of the results of Benediktsdóttir *et al.* (2017). The eigenfunctions of fundamental-mode surface waves with that wavelength have energy concentrated in the top 0.5–1 km of the crust (extrapolating eigenfunctions from Benediktsdóttir *et al.* 2017; Jeddi *et al.* 2017). Thus, if the surface waves are fundamental mode, they are most effectively excited quite near the surface, that is approximately in the top kilometre or less. If they consisted of higher modes, the group velocity would be expected to be higher than that which best concentrates the likelihood of epicentral locations (1.3 km s^{-1}). Therefore, we estimate that the source lies in the top 1 km of the crust.

With the tremor dominated by surface waves, we cannot determine the depth of its source (other than to constrain it through the depth distribution of their eigenfunctions). If the tremor contained a significant component of body waves, then the depth of that component could possibly be determined based on the amplitude distribution with distance by matching that with the distance behaviour predicted by a 1-D velocity model. Similarly, the depth could be estimated using the differential-time information contained in correlograms by back projecting them, or their rendition as a probability density, in 3-D using a traveltime table based on the same 1-D model. In general, this would require more data and it does require substantial knowledge about the average velocity model. Ideally, the velocity model should be three dimensional. Using differential-phase information in this way becomes ambiguous in that it becomes difficult to distinguish a correlation peak of a minor component of the wave field and a secondary scattered arrival if the scattering process is not perfectly diffuse (uniform, dense and isotropic). Estimating depth from amplitudes or power has many degrees of freedom (including the velocity model) and typically involves relatively few data. It also becomes ambiguous in that the tremor may contain both P and S waves and the effects of a scattering process on polarity remains unclear. We have not attempted this with the Eyjafjallajökull data.

We find that the power in the tremor was generally stronger on the vertical component than the horizontals, although the power on the three components is sometimes comparable. This is consistent with tremor containing both Rayleigh and Love waves since the definition of both becomes unclear in a scattering medium. If the tremor consisted of body waves this would imply significant P-wave content. Instantaneous particle motion is not diagnostic of this in a strongly scattering medium at high frequency. For example, Neuberg *et al.* (1994) demonstrated failure of the particle motion of P waves at Stromboli volcano to point to the source at frequencies higher than about 0.5 Hz and very short distance (1500 m). Neither is time-averaged particle motion diagnostic, since the same interference pattern of scattered surface waves is present at all times if the source remains stationary and the medium does not change with time.

8 CONCLUSIONS

We have described, analysed the amplitude of, and located the tremor associated with the 2010 Eyjafjallajökull summit eruption based on differential-phase information. The main conclusions are:

(i) The character of eruptive tremor during the 2010 Eyjafjallajökull eruption resembled that during many other eruptions in Icelandic volcanoes. It was continuous in time with varying amplitude and distributed in frequency between about 0.5 and 5 or 10 Hz, depending on station distance and eruptive character (Fig. 3).

(ii) Low tremor levels when plume height is large during explosive phase of the eruption and high tremor levels when plume height is small during the effusive phase of the eruption. This suggests that effusion generated tremor more efficiently than explosive activity at the surface in the 2010 eruption of Eyjafjallajökull.

(iii) The low-frequency tremor (0.5–2 Hz) emanated from a single dominant source epicentre, which cannot be distinguished from the main eruption site throughout the course of the eruption.

(iv) Tremor bursts during the first days of the eruption do not distinguish themselves from the epicentral location of the tremor as a whole. Instead, both tremor bursts and floods appear to be a consequence of enhanced eruptive activity, or opening of new vents which increased ice melting.

(v) Observed variation with time of power ratios at all stations is most likely due to changes in the radiation of the source.

(vi) The path averaged attenuation quality factor is $Q \approx 10-20$ for some of the nearby stations and $Q \approx 20-50$ for the distal stations based on the vertical component. It is somewhat lower for the horizontal components indicating that the tremor consists of a mix of Love and Rayleigh waves and that the quality factor is lower for Love than Rayleigh waves.

(vii) The 2010 Eyjafjallajökull tremor consisted mostly of surface waves with a source at less than 1 km depth.

ACKNOWLEDGEMENTS

DATA AVAILABILITY

The code used to locate the tremor is available upon request from the fourth author. The raw time series from the temporary seismic stations, correlograms and power spectral densities are available upon request to first author. The raw time series from the SIL-stations (permanent stations) are available upon request to the Iceland Meteorological Office.

REFERENCES

Ágústsdóttir, T. *et al.*, 2016. Strike-slip faulting during the 2014 Bárdarbunga-Holuhraun dike intrusion, central Iceland, *Geophys. Res. Lett.,* **43**(4), 1495–1503.

Ágústsdóttir, T., Winder, T., Woods, J., White, R.S., Greenfield, T. & Brandsdóttir, B., 2019. Intense seismicity during the 2014–2015 Bárdarbunga-Holuhraun rifting event, iceland, reveals the nature of dike-induced earthquakes and caldera collapse mechanisms, *J. geophys. Res.,* **124**(8), 8331–8357.

Aki, K., Fehler, M. & Das, S., 1977. Source mechanism of volcanic tremor: fluid-driven crack models and their application to the 1963 Kilauea eruption, *J. Volc. Geotherm. Res.,* **2**(3), 259–287.

Alparone, S., Andronico, D., Lodato, L. & Sgroi, T., 2003. Relationship between tremor and volcanic activity during the Southeast Crater eruption on Mount Etna in early 2000, *J. geophys. Res.,* **108**(B5), doi:10.1029/2002JB001866.

Arason, P., Petersen, G. & Bjornsson, H., 2011. Observations of the altitude of the volcanic plume during the eruption of Eyjafjallajökull, April-May 2010, *Earth Syst. Sci. Data,* **3**(1), 9–17.

Ballmer, S., Wolfe, C.J., Okubo, P.G., Haney, M. & Thurber, C.H., 2013. Ambient seismic noise interferometry in Hawai'i reveals long-range observability of volcanic tremor, *Geophys. J. Int.,* **194**(1), 512–523.

Baptie, B., Luckett, R. & Neuberg, J., 2002. Observations of low-frequency earthquakes and volcanic tremor at Soufrière Hills Volcano, Montserrat, *Geol. Soc., Lond., Memoirs,* **21**(1), 611–620.

Battaglia, J. & Aki, K., 2003. Location of seismic events and eruptive fissures on the Piton de la Fournaise volcano using seismic amplitudes, *J. geophys. Res.,* **108**(B8), doi:10.1029/2002JB002193.

Battaglia, J., Aki, K. & Ferrazzini, V., 2005. Location of tremor sources and estimation of lava output using tremor source amplitude on the Piton de la Fournaise volcano: 1. Location of tremor sources, *J. Volc. Geotherm. Res.,* **147**(3–4), 268–290.

Benediktsdóttir, Á., Gudmundsson, O., Brandsdóttir, B. & Tryggvason, A., 2017. Ambient noise tomography of Eyjafjallajökull volcano, Iceland, *J. Volcanol. Geotherm. Res.,* **347,** 250–263.

Bianco, F., Castellano, M., Del Pezzo, E. & Ibanez, J.M., 1999. Attenuation of short-period seismic waves at Mt Vesuvius, Italy, *Geophys. J. Int.,* **138**(1), 67–76.

Brandsdóttir, B. & Einarsson, P., 1992. Volcanic tremor and low-frequency earthquakes in Iceland, in *Volcanic Seismology,* pp. 212–222, Springer.

Cannata, A., Catania, A., Alparone, S. & Gresta, S., 2008. Volcanic tremor at Mt. Etna: inferences on magma dynamics during effusive and explosive activity, *J. Volc. Geotherm. Res.,* **178**(1), 19–31.

Caudron, C. *et al.*, 2018. Seismic amplitude ratio analysis of the 2014–2015 Bár arbunga-Holuhraun dike propagation and eruption, *J. geophys. Res.,* **123**(1), 264–276.

Chouet, B., 1985. Excitation of a buried magmatic pipe: a seismic source model for volcanic tremor, *J. geophys. Res.,* **90**(B2), 1881–1893.

Dahm, T. & Brandsdóttir, B., 1997. Moment tensors of microearthquakes from the Eyjafjallajökull volcano in South Iceland, *Geophys. J. Int.,* **130**(1), 183–192.

Del Pezzo, E., Bianco, F. & Zaccarelli, L., 2006. Separation of Qi and Qs from passive data at Mt. Vesuvius: a reappraisal of the seismic attenuation estimates, *Phys. Earth planet. Int.,* **159**(3–4), 202–212.

Di Grazia, G., Falsaperla, S. & Langer, H., 2006. Volcanic tremor location during the 2004 Mount Etna lava effusion, *Geophys. Res. Lett.,* **33**(4).

Droznin, D.V., Shapiro, N.M., Droznina, S.Y., Senyukov, S.L., Chebrov, V.N. & Gordeev, E.I., 2015. Detecting and locating volcanic tremors on the Klyuchevskoy group of volcanoes (Kamchatka) based on correlations of continuous seismic records, *Geophys. J. Int.,* **203**(2), 1001–1010.

Eibl, E.P.S., Bean, C., Jónsdóttir, I., Höskuldsson, A., Thordarson, T., Coppola, D., Witt, T. & Walter, T., 2017a. Multiple coincident eruptive seismic tremor sources during the 2014–2015 eruption at Holuhraun, Iceland, *J. geophys. Res.,* **122**(4), 2972–2987.

Eibl, E.P.S., Bean, C.J., Vogfjörd, K.S., Ying, Y., Lokmer, I., Möllhoff, M., O'Brien, G.S. & Pálsson, F., 2017b. Tremor-rich shallow dyke formation followed by silent magma flow at Bárdarbunga in Iceland, *Nat. Geosci.,* **10**(4), 299–304.

Eibl, E.P.S., Bean, C.J., Einarsson, B., Pálsson, F. & Vogfjörd, K.S., 2020. Seismic ground vibrations give advanced early-warning of subglacial floods, *Nat. Commun.,* **11**(1), 1–11.

Einarsson, P., 2018. Short-term seismic precursors to Icelandic eruptions 1973-2014., *Front. Earth Sci.,* **6,** 45.

Einarsson, P. & Brandsdóttir, B., 1984. Seismic activity preceding and during the 1983 volcanic eruption in Grímsvötn, Iceland, *Jökull,* **34,** 13–23.

Einarsson, P. & Hjartardóttir, Á.R., 2015. Structure and tectonic position of the Eyjafjallajökull volcano, S. Iceland, *Jökull,* **65,** 1–16.

Einarsson, P., Brandsdóttir, B., Gudmundsson, M.T., Björnsson, H., Grönvold, K. & Sigmundsson, F., 1997. Center of the Iceland hotspot experiences volcanic unrest, *Eos,* **78**(35), 369–375.

Fee, D., Haney, M.M., Matoza, R.S., Van Eaton, A.R., Cervelli, P., Schneider, D.J. & Iezzi, A.M., 2017. Volcanic tremor and plume height hysteresis from Pavlof Volcano, Alaska, *Science,* **355**(6320), 45–48.

Fehler, M., 1983. Observations of volcanic tremor at Mount St. Helens volcano, *J. geophys. Res.,* **88**(B4), 3476–3484.

Fujita, E., 2008. Banded tremor at Miyakejima volcano, Japan: implication for two-phase flow instability, *J. geophys. Res.,* **113**(B4), doi:10.1029/2006JB004829.

Furumoto, M., Kunitomo, T., Inoue, H., Yamada, I., Yamaoka, K., Ikami, A. & Fukao, Y., 1990. Twin sources of high-frequency volcanic tremor of Izu-Oshima Volcano, Japan, *Geophys. Res. Lett.,* **17**(1), 25–27.

Furumoto, M., Kunitomo, T., Inoue, H. & Yamaoka, K., 1992. Seismic image of the volcanic tremor source at Izu-Oshima volcano, Japan, in *Volcanic Seismology,* pp. 201–211, eds Gasparini, P., Scarpa, R., Aki, K., Springer.

Gottschämmer, E. & Surono, I., 2000. Locating tremor and shock sources recorded at Bromo Volcano, *J. Volc. Geotherm. Res.,* **101**(1), 199–209.

Gudmundsson, M. *et al.*, 2012. Ash generation and distribution from the April-May 2010 eruption of Eyjafjallajökull, Iceland, *Scient. Rep.,* **2,** 572.

Gudmundsson, M.T., Pedersen, R., Vogfjörd, K., Thorbjarnardóttir, B., Jakobsdóttir, S. & Roberts, M.J., 2010. Eruptions of Eyjafjallajökull Volcano, Iceland, *EOS, Trans. Am. geophys. Un.,* **91**(21), 190–191.

Gudmundsson, Ó. & Brandsdóttir, B., 2010. Geothermal noise at Ölkelduháls, SW Iceland, *Jökull,* **60,** 89–102.

Gudmundsson, Ó., Finlayson, D.M., Itikarai, I., Nishimura, Y. & Johnson, W.R., 2004. Seismic attenuation at Rabaul volcano, Papua new Guinea, *J. Volc. Geotherm. Res,* **130**(1–2), 77–92.

Haney, M.M., 2010. Location and mechanism of very long period tremor during the 2008 eruption of Okmok Volcano from interstation arrival times, *J. geophys. Res.,* **115**(B10), doi:10.1029/2010JB007440.

Hidayati, S., Ishihara, K. & Iguchi, M., 2007. Volcano-tectonic earthquakes during the stage of magma accumulation at the Aira caldera, southern Kyushu, Japan, *Bull. Volcanol. Soc. Jpn.,* **52**(6), 289–309.

Hjaltadóttir, S., Vogfjörd, K.S., Hreinsdóttir, S. & Slunga, R., 2015. Reawakening of a volcano: activity beneath Eyjafjallajökull volcano from 1991 to 2009, *J. Volc. Geotherm. Res.,* **304,** 194–205.

Hofstetter, A. & Malone, S.D., 1986. Observations of volcanic tremor at Mount St. Helens in April and May 1980, *Bull. seism. Soc. Am.,* **76**(4), 923–938.

Hooper, A., Pedersen, R. & Sigmundsson, F., 2009. Constraints on magma intrusion at Eyjafjallajökull and Katla volcanoes in Iceland, from time series SAR interferometry, in *The VOLUME Project–Volcanoes: Understanding Subsurface Mass Movement,* pp. 13–24, eds Bean, C.J., et al., University College.

Hotovec, A.J., Prejean, S. G.and Vidale J.E. & Gomberg, J., 2013. Strongly gliding harmonic tremor during the 2009 eruption of Redoubt Volcano, *J. Volc. Geotherm. Res.,* **259,** 89–99.

Hurst, A.W., 1992. Stochastic simulation of volcanic tremor from Ruapehu, *J. Volc. Geotherm. Res.,* **51**(3), 185–198.

Icelandic Meteoroglogical Office, 2019a. Database of the Icelandic Meteoroglogical Office, afgreidsla nr. 2019-03-01/01.

Icelandic Meteoroglogical Office, 2019b. Database of the Icelandic Meteoroglogical Office, afgreidsla nr. 2019-02-11/01.

Jakobsdóttir, S.S., 2008. Seismicity in Iceland: 1994–2007, *Jökull,* **58,** 75–100.

Jeddi, Z., Tryggvason, A. & Gudmundsson, Ó., 2016. The Katla volcanic system imaged using local earthquakes recorded with a temporary seismic network, *J. geophys. Res.,* **121**(10), 7230–7251.

Jeddi, Z., Gudmundsson, Ó. & Tryggvason, A., 2017. Ambient-noise tomography of Katla volcano, south Iceland, *J. Volc. Geotherm. Res.,* **347,** 264–277.

Jónsson, B., 1774. *Annalar Thess Froma og velvitra Sauluga Biørns Jonssonar a Skardsau Fordum Løgrettumanns i Hegranes-sýslu,* Skardsárannáll, Available at: http://baekur.is/bok/000043701/Annalar_T Hess_froma_og.

Julian, B.R., 1994. Volcanic tremor: nonlinear excitation by fluid flow, *J. geophys. Res.,* **99**(B6), 11 859–11 877.

Karlsdóttir, S., Gylfason, Á.G., Höskuldsson, Á., Brandsdóttir, B., Ilyinskaya, E., Gudmundsson, M.T. & Högnadóttir, T., 2012. in *The 2010 Eyjafjallajökull eruption, Iceland, IMO, IES and NCIP-DCPEM Rport to ICAO 2012,* p. 209.

Konstantinou, K.I. & Schlindwein, V., 2003. Nature, wavefield properties and source mechanism of volcanic tremor: a review, *J. Volc. Geotherm. Res.,* **119**(1), 161–187.

Kumagai, H. *et al.*, 2010. Broadband seismic monitoring of active volcanoes using deterministic and stochastic approaches, *J. geophys. Res.,* **115**(B8), doi:10.1029/2009JB006889.

Kumagai, H., Londoño, J.M., Maeda, Y., López Velez, C.M. & Lacson, R. Jr, 2018. Envelope widths of volcano-seismic events and seismic scattering characteristics beneath volcanoes, *J. geophys. Res.,* **123**(11), 9764–9777.

Larsen, G., Dugmore, A. & Newton, A., 1999. Geochemistry of historical-age silicic tephras in Iceland, *Holocene,* **9**(4), 463–471.

Li, K.L. & Gudmundsson, O., 2020. A probabilistic tremor location method, *Geophys. Res. Lett.,* **47**(4), e2019GL085538.

Li, K.L., Sadeghisorkhani, H., Sgattoni, G., Gudmundsson, O. & Roberts, R., 2017a. Locating tremor using stacked products of correlations, *Geophys. Res. Lett.,* **44**(7), 3156–3164.

Li, K.L., Sgattoni, G., Sadeghisorkhani, H., Roberts, R. & Gudmundsson, O., 2017b. A double-correlation tremor-location method, *Geophys. J. Int.,* **208**(2), 1231–1236.

Magnússon, E., Gudmundsson, M.T., Roberts, M.J., Sigurdsson, G., Höskuldsson, F. & Oddsson, B., 2012. Ice-volcano interactions during the 2010 Eyjafjallajökull eruption, as revealed by airborne imaging radar, *J. geophys. Res.,* **117**(B7), doi:10.1029/2012JB009250.

McNutt, S.R., 1992. Volcanic tremor, *Encycloped. Earth Syst. Sci.,* **4,** 417–425.

Métaxian, J.P., Lesage, P. & Dorel, J., 1997. Permanent tremor of Masaya Volcano, Nicaragua: wave field analysis and source location, *J. geophys. Res.,* **102**(B10), 22 529–22 545.

Morioka, H., Kumagai, H. & Maeda, T., 2017. Theoretical basis of the amplitude source location method for volcano-seismic signals, *J. geophys. Res.,* **122**(8), 6538–6551.

Neuberg, J., Luckett, R., Ripepe, M. & Braun, T., 1994. Highlights from a seismic broadband array on Stromboli volcano, *Geophys. Res. Lett.,* **21**(9), 749–752.

Neuberg, J., Luckett, R., Baptie, B. & Olsen, K., 2000. Models of tremor and low-frequency earthquake swarms on Montserrat, *J. Volc. Geotherm. Res.,* **101**(1–2), 83–104.

Oddsson, B., Gudmundsson, M.T., Edwards, B.R., Thordarson, T., Magnússon, E. & Sigurdsson, G., 2016. Subglacial lava propagation, ice melting and heat transfer during emplacement of an intermediate lava flow in the 2010 Eyjafjallajökull eruption, *Bull. Volcanol.,* **78**(7), 48.

Óskarsson, B.V., 2009. *The Skerin ridge on Eyjafjallajökull, south Iceland: Morphology and magma-ice interaction in an ice-confined silicic fissure eruption, Master's thesis,* Faculty of Earth Sciences, University of Iceland, Available at: http://hdl.handle.net/1946/4375.

Pedersen, R. & Sigmundsson, F., 2004. InSAR based sill model links spatially offset areas of deformation and seismicity for the 1994 unrest episode at Eyjafjallajökull volcano, Iceland, *Geophys. Res. Lett.,* **31**(14),.

Pedersen, R. & Sigmundsson, F., 2006. Temporal development of the 1999 intrusive episode in the Eyjafjallajökull volcano, Iceland, derived from InSAR images, *Bull. Volcanol.,* **68**(4), 377–393.

Pedersen, R., Sigmundsson, F. & Einarsson, P., 2007. Controlling factors on earthquake swarms associated with magmatic intrusions: constraints from Iceland, *J. Volc. Geotherm. Res.,* **162**(1-2), 73–80.

Ripepe, M., 1996. Evidence for gas influence on volcanic seismic signals recorded at Stromboli, *J. Volc. Geotherm. Res.,* **70**(3), 221–233.

Schlindwein, V., Wassermann, J. & Scherbaum, F., 1995. Spectral analysis of harmonic tremor signals at Mt. Semeru volcano, Indonesia, *Geophys. Res. Lett.,* **22**(13), 1685–1688.

Sgattoni, G., Gudmundsson, Ó., Einarsson, P., Lucchi, F., Li, K.L., Sadeghisorkhani, H., Roberts, R. & Tryggvason, A., 2017. The 2011 unrest at Katla volcano: characterization and interpretation of the tremor sources, *J. Volc. Geotherm. Res.,* **338,** 63–78.

Sigmarsson, O. *et al.*, 2011. Remobilization of silicic intrusion by mafic magmas during the 2010 Eyjafjallajökull eruption, *Solid Earth,* **2**(2), 271–281.

Sigmundsson, F. *et al.*, 2010. Intrusion triggering of the 2010 Eyjafjallajökull explosive eruption, *Nature,* **468**(7322), 426–430.

Sigtryggsson, H. & Sigurdsson, E., 1966. Earth tremors from the Surtsey eruption 1963–1965, *Surtsey Res. Prog. Rep.,* **2,** 131–138.

Soosalu, H., Einarsson, P. & Thorbjarnardóttir, B.S., 2005. Seismic activity related to the 2000 eruption of the Hekla volcano, Iceland, *Bull. Volc.,* **68**(1), 21–36.

Sturkell, E., Sigmundsson, F. & Einarsson, P., 2003. Recent unrest and magma movements at Eyjafjallajökull and Katla volcanoes, Iceland, *J. geophys. Res.,* **108**(B8), doi:10.1029/2001JB000917.

Tarasewicz, J., White, R.S., Brandsdóttir, B. & Thorbjarnardóttir, B., 2011. Location accuracy of earthquake hypocentres beneath Eyjafjallajökull, Iceland, prior to the 2010 eruptions, *Jökull,* **61**, 33–50.

Tarasewicz, J., Brandsdóttir, B., White, R.S., Hensch, M. & Thorbjarnardóttir, B., 2012a. Using microearthquakes to track repeated magma intrusions beneath the Eyjafjallajökull stratovolcano, Iceland, *J. geophys. Res.,* **117**(B9), doi:10.1029/2011JB008751.

Tarasewicz, J., White, R.S., Woods, A.W., Brandsdóttir, B. & Gudmundsson, M.T., 2012b. Magma mobilization by downward-propagating decompression of the Eyjafjallajökull volcanic plumbing system, *Geophys. Res. Lett.,* **39**(19).

Tarasewicz, J., White, R.S., Brandsdóttir, B. & Schoonman, C.M., 2014. Seismogenic magma intrusion before the 2010 eruption of Eyjafjallajökull volcano, Iceland, *Geophys. J. Int.,* **198**(2), 906–921.

Thompson, G., McNutt, S.R. & Tytgat, G., 2002. Three distinct regimes of volcanic tremor associated with the eruption of Shishaldin Volcano, Alaska 1999, *Bull. Vol.,* **64**(8), 535–547.

Thorarinsson, S., Steinthórsson, S., Einarsson, T., Kristmannsdottir, H. & Oskarsson, N., 1973. The eruption on Heimaey, Iceland, *Nature,* **241**(5389), 372.

Vogfjörd, K.S. *et al.*, 2005. Forecasting and monitoring a subglacial eruption in Iceland, *EOS, Trans. Am. geophys. Un.,* **86**(26), 245–248.

Wassermann, J., 1997. Locating the sources of volcanic explosions and volcanic tremor at Stromboli volcano (Italy) using beam-forming on diffraction hyperboloids, *Phys. Earth planet. Inter.,* **104**(1–3), 271–281.

Wessel, P., Smith, W.H.F., Scharroo, R., Luis, J. & Wobbe, F., 2013. Generic mapping tools: improved version released, *EOS, Trans. Am. geophys. Un.,* **94**, 409–410.

Woods, J., Donaldson, C., White, R.S., Caudron, C., Brandsdóttir, B., Hudson, T.S. & Ágústsdóttir, T., 2018. Long-period seismicity reveals magma pathways above a laterally propagating dyke during the 2014–15 Bárdarbunga rifting event, Iceland, *Earth planet. Sci. Lett.,* **490,** 216–229.

SUPPORTING INFORMATION

Supplementary data are available at *GJIRAS* online.

tremor_eyja_aug2021_appendix.pdf

Please note: Oxford University Press is not responsible for the content or functionality of any supporting materials supplied by the authors. Any queries (other than missing material) should be directed to the corresponding author for the paper. Supplementary material. The one I sent in had captions for all figures.